Universidad de Concepción
Dirección de Postgrado
Facultad de Ciencias Físicas y Matemáticas – Programa de Magíster en Ciencias con Mención en Física

Kinematics of the Inner Kiloparsec of the Seyfert 2 Galaxy ESO153-g20

(Cinemática de la galaxia Seyfert ESO153-g20)

Tesis para optar al grado de Magíster en Ciencias con mención en Física

Pamela Raquel Soto Pinto
Concepción – Chile
2018

Profesor Guía: Dr. Neil Mark Nagar
Dpto. de Astronomía, Facultad de Ciencias Físicas y Matemáticas
Universidad de Concepción

Agradecimientos

Debo decir que son muchas las personas a quiénes me gustaría agradecer por todo el apoyo brindado en estos años, pero empezaré por los más importantes: mi familia. Su apoyo ha sido siempre incondicional, desde el momento en que se me ocurrió estudiar astronomía. Gracias a mis padres, por no tratar de cambiar el rumbo que elegí, por su cariño incomparable y sobre todo por el ánimo que me han dado siempre para poder cumplir mis sueños. A mis hermanos, por estar presentes aunque no entendieran nada de lo que les hablaba y por hacerme reir cuando era necesario. A mis abuelos: mi Mamama y tío Milton, por siempre mantener esa curiosidad en lo que estudio y lo que me apasiona, pero sobre todo por mantenerme al día con las noticias astronómicas que no siempre me enteraba a pesar de estar estudiando sobre ello. A mi tata y su familia por el apoyo y energía que me entregaron siempre. A mi abuelita Anita y mi tata Luis, por mostrar interés siempre y darme ánimos para seguir. Tatita, nos dejaste antes que esta tesis terminara, pero siempre estuviste presente a tu manera y te agradezco por eso.

Otro grupo importante a quien debo agradecer son mis amigos: aquellos incondicionales que me ha dado la vida a lo largo de los años y que, a pesar de cada uno seguir su propio camino, siempre están presentes en los momentos necesarios. Muchas gracias a todos, en especial a Dania, por ser la mejor amiga durante estos 7 años de aventura; a Ginette, Natalia (Naty) y Jocelyn, porque a pesar de habernos separado un poco en estos años debido a diversas razones, siempre han estado presentes en este proceso; a Aldo, Carla y Camila (Chumbe) por siempre dar ánimos en la sala, ya fuera poniendo música o incluso distrayendo un poco a la gente; a Sarai, Natalia Machuca, Claudio y Ángela (Angie), por ofrecerme su linda amistad en estos años de universidad.

No puedo olvidar tampoco a mis incondicionales del colegio: a Marcelo (Chelo), por siempre molestar cuando uno le decía que estaba trabajando en la tesis o con clases y el sacaba pica por haber terminado y estar trabajando; a Jorge Landaeta, quien se integró a este grupo gracias al Chelo y siempre tiene alguna buena historia que contar; a Javier (Pack) y Romina, porque a pesar que nos hemos visto poco últimamente, siempre se las arreglan para estar en momentos importantes y apoyar cuando es necesario. Finalmente, agradezco a Jorge Torres, el más incondicional de todos, y ahora mi partner de vida, por siempre estar en esta aventura y acompañarme en todo momento.

A ambos grupos, no olvidaré jamás las risas sin motivo alguno y los momentos difíciles en los que siempre supieron hacerme sentir mejor. Los adoro de verdad.

Resumen

El estudio de la cinemática del gas en galaxias cercanas ha sido parte de diversos trabajos [31, 60, 89–91, 101], en búsqueda de indicios de inflows o outflows de gas hacia o desde el núcleo, para poder entender cuáles son los mecanismos responsables de transferir masa desde escalas galácticas hasta escalas nucleares para alimentar el agujero negro supermasivo (SMBH). Esto se debe a que está ampliamente aceptado que la radiación emitida por un núcleo activo galáctico (AGN) corresponde al resultado de la acreción sobre su SMBH en un rango de masas $\sim 10^6$-$10^9\,M_\odot$ [4, 62]. La búsqueda de estos indicadores ha sido motivada (en los últimos años) por el descubrimiento de Lopes (2007) [95] de que hay una marcada diferencia en el contenido de polvo y gas de esta región en galaxias activas de tipo temprano cuando se comparan con galaxias no activas: mientras las primeras siempre presentan estructuras compactas, en la forma de brazos espirales y/o filamentos a escalas de cientos de parsecs; sólo un 25 por ciento de las no activas tienen dichas estructuras. Esto indica que una reserva de gas y polvo es una condición necesaria para la actividad nuclear, y también sugiere que las estructuras compactas son indicadores de vías de alimentación hacia el AGN [89, 90].

Esta tesis es otro estudio observacional en este campo, donde el caso de la galaxia cercana Seyfert 2 ESO 153-g20 es investigado, analizando la cinemática estelar y gaseosa de sus 1.4×1.9 kpc^2 centrales. Mientras la cinemática estelar no presenta características interesantes más que aquellas asociadas a la rotación del disco galáctico, la cinemática del gas muestra una importante componente adicional, claramente observada en la mayoría de las líneas de emisión más fuertes provenientes de gases más volátiles y, por tanto, más propensos a ser alterados por un agente externo o reciente, como un flujo hacia afuera o hacia adentro. En nuestro caso, asociamos dicha componente a un flujo hacia afuera (outflow), el que solo puede ser observado en un lado de la galaxia. Debido a la resolución de nuestros datos, pudimos estimar la tasa de flujo de masa del outflow y la tasa de acreción hacia el SMBH. Además, usando la dispersión de las estrellas, se estimó la masa del SMBH utilizando la relación M-σ.

Los resultados obtenidos servirán para aumentar la muestra de galaxias que han sido estudiadas cinemáticamente hasta ahora; ayudando a mejorar las condiciones iniciales que se usan en simulaciones o a obtener mejores diferencias entre los distintos tipos de galaxias, ya sean activas o no, para así lograr tener un mejor entendimiento de la evolución de estos objetos.

Abstract

The study of gas kinematics in nearby galaxies has been part of different works [31, 60, 89–91, 101], searching for signatures of gas inflows and/or outflows to/from the nucleus in order to understand the mechanisms responsible for transfering mass from galactic scales down to nuclear scales to feed the supermassive black hole (SMBH). This is because it is widely accepted that the radiation emitted by an active galactic nucleus (AGN) is a result of the accretion on to the SMBH in the mass range $\sim 10^6$-$10^9\,M_\odot$ [4, 62]. The searching of this signatures has been motivated (in the last few years) by the finding of Lopes (2007) [95] that there is a marked difference in the dust and gas content of this regions in early-type active galaxies when compared to non-active ones: while the first always have dusty structures, in the form of spiral and filaments at hundreds of parsecs scales, only 25 per cent of the non-active ones have such structures. This indicates that a reservoir of gas and dust is a necessary condition for the nuclear activity and also suggests that the dusty structures are tracers of feeding channels to the AGN [89, 90].

The present thesis is another observational study on this field, where the case of the nearby Seyfert 2 galaxy ESO 153-g20 is investigated, analyzing the stellar and gaseous kinematics of its inner 1.4×1.9 kpc^2. While the stellar kinematics does not present interesting features more than those associated with the pure rotation of the galactic disk, the gaseous kinematics show an important additional component, well observed in the majority of the stronger emission lines which come from more volatile gases and, therefore, more likely to be altered by an external or recent factor such an outflow/inflow event. In our case, we associated this second component to an outflow, which can only be observed on one side of the galaxy. Due to the resolution of our data, we were able to estimate the mass outflow rate and the accretion rate onto the SMBH. In addition, using the stellar dispersion, the mass of the SMBH was estimated using the M-σ relation.

The results obtained will serve to increase the sample of galaxies that have been kinematically studied so far; helping to improve the initial conditions used in simulations or to obtain better differences between the different types of galaxies, being them active or not, in order to attempt a better understanding on the evolution of these objects.

Contents

List of Figures

List of Tables

Chapter 1

Introduction

1.1 Morphological Classification of Galaxies

Galaxies are found in a variety of properties and shapes, creating the special need of classifying them into different morphological types to study their properties in a better way. One of the first and well-known classification of galaxies is the Hubble sequence (also known as the Hubble tuning fork diagram) [48], which can be seen on figure 1.1. In this work, Hubble classified the galaxies he observed into four different categories: ellipticals, lenticulars, spirals (which are subdivided into barred and nonbarred) and irregular galaxies.

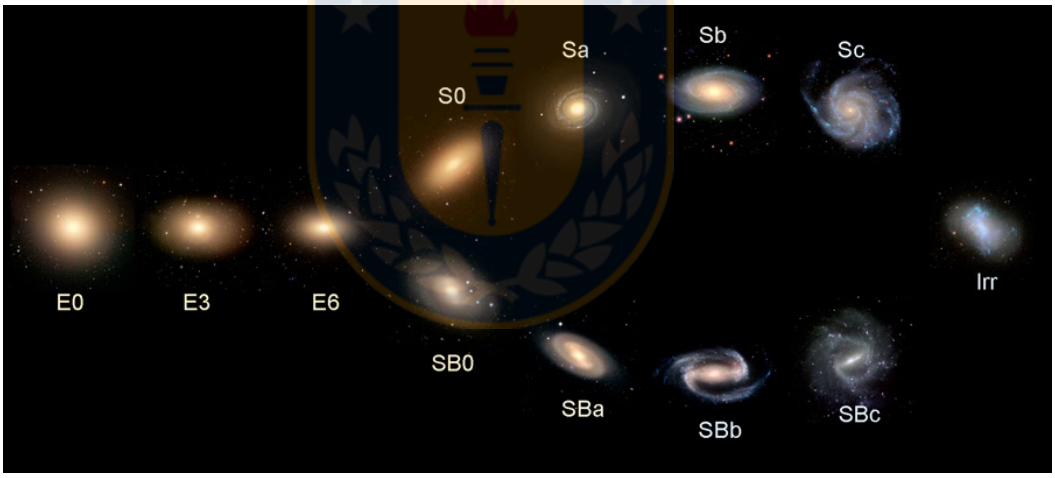

Figure 1.1: Hubble's Galaxy Classification Scheme is presented. On this thesis, we studied a SBab galaxy, which corresponds to a barred spiral galaxy. Image taken from the Galaxy Zoo forum.

He gave the elliptical galaxies numbers from zero to seven, according to their ellipticity: "E0" is round (or almost) and "E7" is elliptical (or cigar shaped); the last representing a limiting figure which marks the junction with spiral galaxies. In the case of spirals, they were assigned letters from "a" to "c" attached to the spiral symbol "S". These three letters characterize the compactness of their spiral arms and the relative size of the nucleus: "Sa" spirals are tightly wound and most of the nebulosity is in the nuclear region while "Sc" spirals are the most open and show an inconspicuous nucleus.

Barred spirals are contracted with the symbol "SB" and the most important difference with the previous type is the bar of stars that appears on the central bulge. The arms usually start at the end of the bar instead of from the bulge and their classification follows the same properties as for normal spirals. In the case of "SBa" galaxies, they look like the greek letter θ, while

"SBc" galaxies are represented by the S-shaped spirals.

In the transition zones between ellipticals and spirals appears the "S0" or lenticular galaxies, which are the ones that appear to have a spiral disc but no visible arms.

The last classification corresponds to irregular galaxies, which are the ones that doesn't show an obvious spiral structure or nuclear bulge, looking as a random collection of stars with no obvious order or symmetry.

At the beginning, this classification was thought to be an evolutionary sequence where galaxies might evolve from one type to another, progressing from left to right across the diagram. However, galaxy evolution is a more complex process than Hubble imagined and involves collisions with other galaxies, the galaxy's initial collapse, flow of internal star birth among other properties.

1.2 Active Galactic Nuclei

When we talk about Active Galactic Nuclei, or AGN, we are refering to the existence of high energetic phenomena and non-stellar processes happening in the nucleus of galaxies. It was first defined based on observational characteristics made by Carl Seyfert in 1943, who noticed some additional strongly emitting component in the center of some galaxies. He studied six galaxy spectra showing high-excitation nuclear emission lines superposed on a normal star-like spectrum [93]. Another thing he noticed, was the presence of broad emission lines on some galaxies, while others exhibited only narrow ones; but his work received no further attention until the 1960s, when strong radio sources were discovered with optical counterparts often appeared point-like, leading to the designation of "quasi-stellar objects" (QSOs). Woltjer [113] pointed out that if nuclei are extremely narrow (on the order of 100 pc) and if a normal mass-to-light ratio applies, galaxies would require a mass of a few $10^8\,M_\odot$ to prevent desintegration.

At least half of all known galaxies in the nearby universe host an AGN [50] and are commonly known as "active" galaxies. The two main classes of AGNs are Quasars and Seyfert galaxies, differentiated by the amount of radiation emitted by the compact central source. In the case of a typical Seyfert, the total energy emitted by the nuclear source at optical wavelengths is comparable to the energy that all of the stars in the galaxy emit ($\approx 10^{11}\ L_\odot$), but in a typical quasar the nuclear source is brighter than the stars by a factor of 100 or more, as pointed out on "An introduction to Active Galactic Nuclei" [79].

Netzer (2006, and references therein) [71] pointed out that most of AGN include many of the following components, which can be seen in figure 1.2:

1. An accretion disk, which is a "subparsec rotation-dominated flow". We can observe optically thick or thin disks. The first ones can be geometrically thin (thin accretion disk) or thick (thick or slim accretion disk), while optically thin disks (or flows) are occasionally advection dominated.

2. A broad-line region (BLR), which are high-density, dust-free clouds at distances closer to the black hole (BH), that are moving at roughly Kleperian velocities.

3. The central torus, which corresponds to an axisymmetric dusty structure with luminosity-dependent dimensions of 0.1–10 pc.

4. The narrow-line region (NLR), which are lower-density and lower-velocity ionized gas clouds extending from just outside the torus to hundreds and even thousands of parsecs along the general direction of the opening in the torus (ionization cones). Most of this gas contains dust except for very close in, in a region named as the coronal line region.

5. A very thin molecular maser disk similar in size to the torus.

6. A central radio jet occasionally associated with γ-ray emission.

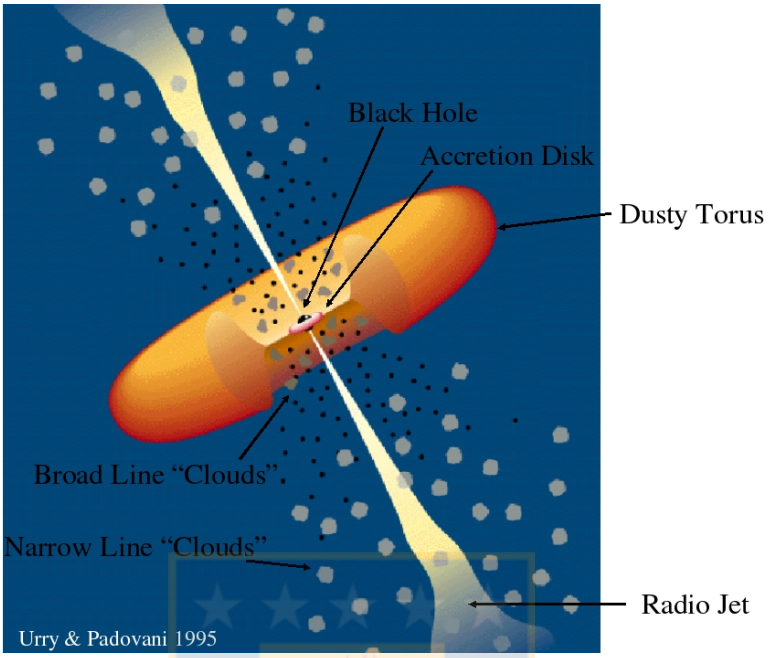

Figure 1.2: AGN scheme. This is a schematic diagram (not to scale) where it is possible to identify the different components of an AGN: the accretion disk that surrounds the central black hole; a thick dusty torus; broad line "clouds", which are orbiting above the disk and perhaps by the disk itself; narrow line "clouds", which are farther from the central source; and the Radio jets, shown as diffuse jets characteristic of low-luminosity, which emanate from the region near the black hole. This image is from Urry & Padovani (1995) [106].

1.2.1 AGN Classification

Many AGNs types have been discovered over the years, which lead to a large variety of subtypes according to different parameters. For example, the mass of the central SMBH can range from 10^5 $M_\odot$, like NGC 4395, up to 10^{10} $M_\odot$, which is the case of the quasar 3C 273. In the case of their bolometric luminosity (L_{bol}), it can range from 10^{41} to 10^{48} erg s^{-1}.

As mentioned on the beginning of this section, the discovery of Carl Seyfert was not very considered until 1959 when Woltjer tried to physically understand what Seyfert pointed out. With the discovery of radio sources and the development of new instruments, more objects have been found at different wavelengths. Below there is a summary of some AGN types and H II regions (see Tadhunter (2008) and Heckman (1980) [43, 104]).

- Seyfert Galaxies: The main difference between Seyfert and non-active galaxies is their quasar-like nuclei with very high surface brightnesses and optical spectra dominated by high-excitation nuclear emission lines, which can show both broad (>1000 km s^{-1}) and narrow (few 100 km s^{-1}) emission lines, called Seyfert 1 galaxies; or only narrow emission lines, called Seyfert 2 galaxies. We can also find intermediate classifications based on the strength in the broad component of Hβ. These are named Seyfert 1.2, 1.5, 1.8 and 1.9, following the scheme introduced by Osterbrock (1977) [74].

- LINERs: Low-ionization nuclear emission-line regions (LINERs) are a type of galactic nuclei that show faint nuclear luminosities and strong emission lines originated from weakly ionized or neutral atoms (like O, O^+, N^+ and S^+). It remains uncertain whether all

LINERs are truly AGNs, or rather a subset of them represent nuclear star-forming regions [45, 46]. Line widths on this type are usually of 200-400 $\mathrm{km\,s^{-1}}$, with properties very similar to Seyfert 2 galaxies but with stronger forbidden lines. They can show [O III]λ5007Å/Hβ < 3. In comparison to H II regions, LINERs have stronger [N II] emission line fluxes than Hα.

- H II regions: Correspond to regions whose emission line spectrum is produced by massive gas clouds of ionized hydrogen. They are detected mostly in spiral, irregular and compact galaxies and always present strong forbidden oxygen lines, with [O III]/Hβ > 3. These objects typically present electron temperatures in the range 5.000-18.000 K and electron densities usually of the order of a few dozen to a few hundred per $\mathrm{cm^{-3}}$. Unlike AGNs, the ionizing sources are massive O and B stars located in star-forming regions instead of an accreting SMBH.

The main differences mentioned above for the types of AGN can be observed in figure 1.3 where three different spectra (one for each type) are shown for comparison.

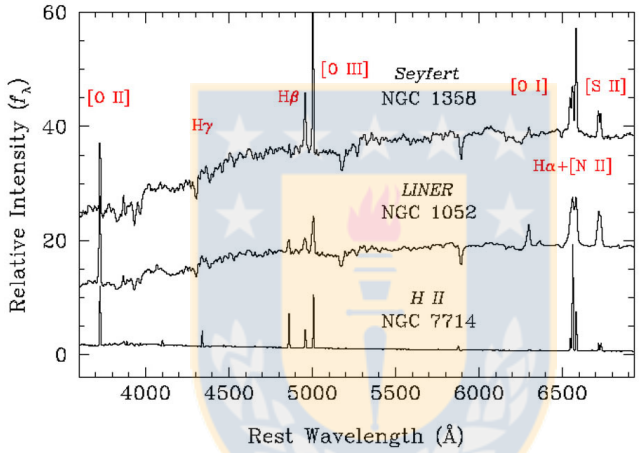

Figure 1.3: Seyfert, LINER and H II spectra: optical sample of various classes of emission-line nuclei and H II regions. Prominent emission lines are labeled. Image based on Ho et al. (1993) [45]

In 1981, Baldwin, Phillips and Terlevich published a set of diagnostic diagrams, of which the most useful to date has been the called "BPT-NII diagram" [2] (see figure 1.4). It use four strong emission lines in the optical wavelength range to distinguish between AGN (Seyfert, LINERs) and star-forming dominated galaxies (H II regions). The choice of such lines allows to avoid contamination by redshift since they are so close in wavelength: Hα with [N II]λ6583 Å and Hβ with [O III] λ5007 Å. Several adjustments have been proposed for this diagram due to the absence or difficulties in obtain some required emission lines [18] or extreme nature in the interstellar medium of galaxies at high redshift ($z \geqslant 1.5$) [53]. This can give rise to ambiguities of classification. That is why other line ratios have also been considerer, such as [S II] and [O I] emission lines.

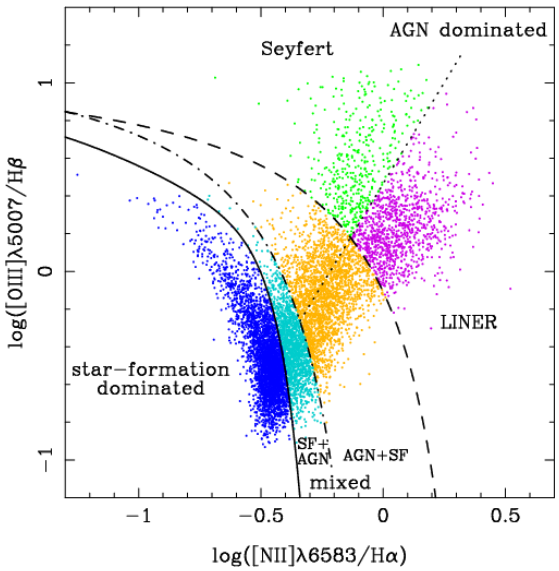

Figure 1.4: Diagnostic diagram example from Bamford (2008) [3]. This is one of the most used versions.

1.2.2 AGN Unified Model

The *old* AGN unification scheme (Antonucci 1993, Urry & Padovani 1995 [1, 106]) proposes that the large diversity of observed AGN properties can be explained two physical parameters: the torus inclination to the line-of-sight (LOS) and the source luminosity. This scheme is perhaps the simplest possible way to characterize the fact that the nuclear continuum and emission line radiation of AGNs can suffer wavelength dependent scattering, absorption and reflection on the way out. This can take place in the torus, in the disk of the host galaxy, in stellar and nuclear outflows, and inside the BLR itself. As example, if we consider the existence of an optically thick torus surrounding the central regions of an AGN on scales of 1-100 pc, it would lead to absence of broad emission lines in the case of Seyfert 2, if observed edge-on, because the broad line region would be hidden. On the other hand, if it is observed face-on, it would lead to a Seyfert 1 galaxy because the BLR would be visible [1, 82]. An scheme of this unified model is shown in Figure 1.5

Netzer (2015) [72] pointed out that recent observations of large AGN samples, and more detailed information about specific sources, lead to the conclusion that this *old* unification scheme requires three major modifications: (1) One related to the physics and structure of the central obscurer, (2) the realization that there are real differences between various sub-groups, further than the dependence on luminosity and torus inclination; and (3) a modification related to BH and galaxy evolution.

1.2.3 Kinematics and dynamics of Galaxies through IFS

Rotation of spiral galaxies was first recognized from the inclination of the stellar absorption lines on spectra of the central regions by Wolf (1914) [112] in M81 and Slipher [97] in M104. An explication of this discovery could be that the central areas are often deficient in the H II regions responsible for the emission lines [108] and also absorption lines had been known for a longer time than the emission ones. Today we have evolved to the common use of Integral Field Spectroscopy (IFS) to measure the motion of gas and stars in the object of interest, in order to better understand the evolution of galaxies. It is vital to observe the kinematic processes that occur in them, from their outer regions down to the regions surrounding the nuclear supermassive black hole (hereafter SMBH). This method fed the signal from each cell

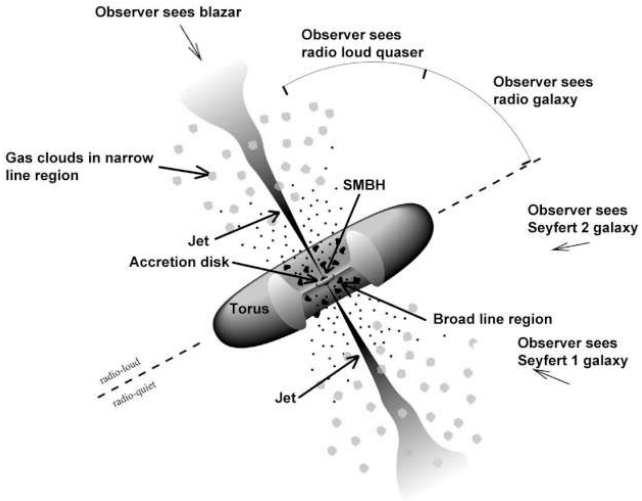

Figure 1.5: AGN unifed model. The type of object that can be seen depends on the orientation of the observer with respect to the accretion disk, the dusty torus, and the jet, as shown in the illustration here. Ilustration from the Fermi telescope webpage (https://fermi.gsfc.nasa.gov/science/eteu/agn/)

or spatial pixel (spaxel) of the field of interest in the sky into a spectrograph equipped with an integral field unit (IFU), which then generates a spectrum for each individual spaxel. All the resulting spectra are arranged into a datacube which contains the entire 2D field of view plus a third dimension drawn from the spectrograph. In Figure 1.6, a scheme showing how a data cube looks like is shown. Some early works that provided two-dimensional gas kinematic maps of the central parts in nearby active galaxies, such as NGC 3227, are: Mediavilla (1993) [65] in optical wavelength; and Davies (2006) [23] in the near-infrared using SINFONI at the Very Large Telescope.

Throughout the results of this thesis, data observed with the Integral Field Unit of the Gemini Multi-Object Spectrograph (GMOS-IFU [37], see Chapter 3) is presented.

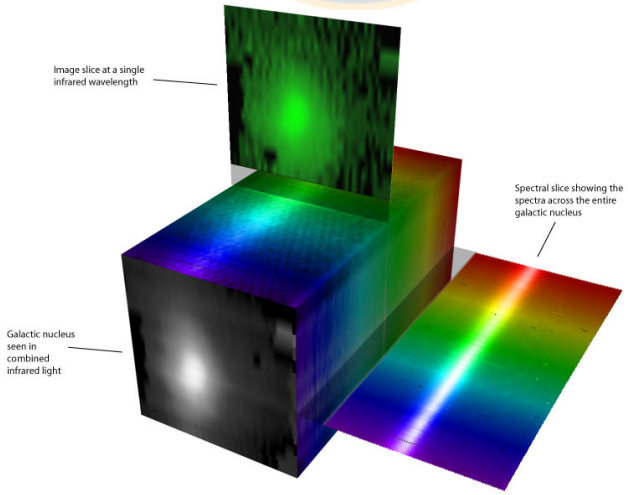

Figure 1.6: Data cube concept showing the 3 dimensions. Credits of the image: Stephen Todd (ROE) and Douglas Pierce-Price (JAC). Taken from http://ifs.wikidot.com/what-is-ifs

It is well known that stars can only change their velocities in a continuous way, by acceleration

due to the gravity, and that, having a small density, they do not interact mostly during a merger event. Then, stellar kinematics can give us a direct information about: the gravitational potential in galaxies and how galaxies were before a merger event.

In galaxies on the immediate surrounding of the the Milky Way, where the light of a single star can't be resolved, the line-of-sight velocity distribution (LOSVD), which corresponds to the probability to find a star in a specific point of the galaxy with a certain projected velocity, contains all the possible information we need. Then, to measure the stellar kinematics it is required to assume that what is seen in a specific galactic spectra is the sum of all contribution of stars inside the spatial resolution and along the line-of-sight. For the case of distant galaxies, contribution of other galaxies or even a cluster have been observed contaminating the original spectrum. The galaxy in study, ESO 153-G20, is a nearby galaxy ($z = 0.019737$), so those contribution can be ignored in this case.

One good way to obtain the stellar kinematic in a galaxy is to convolve stellar or galaxy templates to the observed spectra, expanding the LOSVD as Gauss-Hermite series [36, 109]:

$$\mathcal{L}(\nu) = \frac{e^{-(1/2)y^2}}{\sigma\sqrt{2\pi}}\left[1 + \sum_{m=3}^{M} h_m H_m(y)\right]$$

where $y = (\nu - V)/\sigma$, H_m are the Hermite polynomials and h_m are the Hermite coefficients of which h_3 and h_4 are kinematically important (see below). Finally, the radial velocity, velocity dispersion and other stellar parameters are fitted simultaneously, following the procedure of the Penalized Pixel Fitting technique (pPXF, [15, 17]).

Otherwise, the interstellar gas corresponds to more than 95% of the interstellar medium mass and although it is very dilute (1 atom per cm^3), it is more susceptible to perturbations. For example, if we want to study large-scale interstellar medium kinematics, dark matter, effects of interaction between galaxies and perturbations in the gravitational potential [8, 98, 108], we should observe neutral hydrogen (H I). If our interest are kinematic perturbations coming from, e.g. explosions of super nova or from the AGN and/or inflowing material in a galactic bar, spiral arms or a combination of both; we should observe high ionization gas, like [O III], which is more volatile and can more accurately trace the features mentioned.

The gaseous kinematics information can be extracted using different approaches to its emission lines, of which the most used is the Gaussian profile. The area under the Gaussian correspond to the integrated flux, the wavelength of the Gaussian peak is transformed in the observed velocity using the doppler effect, the width represents the velocity dispersion and, when the resolution is enough, it is also possible to measure inhomogeneities between the Gaussian fit and the real spectra such as the skewness (asymmetry) and kurtosis (degree of peakedness). All these measurements are also known as kinematic moments, where the moment 0 is the flux, moment 1 is the radial velocity (v), moment 2 corresponds to the velocity dispersion (σ); and the skewness and kurtosis are the h_3 and h_4 Gauss-Hermite moments, respectively. For a more detailed explanation of the Gauss-Hermite moments in the kinematic context see, e.g., Riffel (2010) [83].

In order to interpret the observed velocities in a spiral galaxy, it must be assumed that they come from a single inclined plane and its rotation is the dominant pattern. With coordinates R and θ representing the radius and the azimuth angle of the major axis (the intersection between the plane of the sky and the galactic plane), respectively, and an inclination i of the galactic plane. The observed velocities are:

$$V_{obs} = V_{sys} + V(R)sin(i)cos(\theta)$$

When plotting these velocities versus their radial distance along a fixed axis, a rotation curve is constructed. If these velocities are seen in two dimensions, covering an area in a galaxy and not just a specific axis, with contours that mark the regions where the velocities are constant the a contour diagram is obtained, better known as a spider diagram. In Figure 1.7 an example of rotation curve and its corresponding spider diagram are presented.

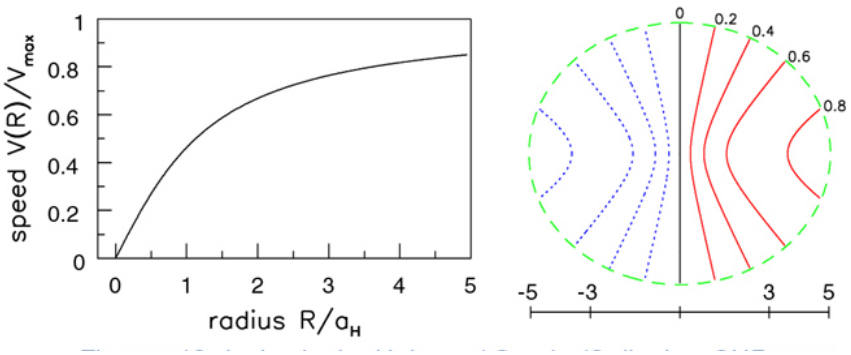

Figure 1.7: Rotation curve and spider diagram example: Rotation curve and its corresponding spider diagram. The velocities are normalized and the radius are divided by a constant number, a_H. Images are from Fig. 5.19 of the book "Galaxies in the Universe" by L. Sparke and J. Gallagher (2007) [99].

The kinematic measurements allow possible construction of position velocity maps, structure maps, velocity fields or maps from all available and credible moments in addition to improvement techniques like the Voronoi binning method [16], which allows to fix a minimal signal-to-noise ratio to the measurements. With the use of velocity fields, for example, it is possible to measure the level of perturbation in the kinematics like changes in the gaseous kinematic major axis along different distances from the nucleus and then compare it with the stellar kinematics to look for differences between active and non-active galaxies [27]. It is also possible to distinguish perturbations due to bars and spirals and use these results to improve hydrodynamic models.

Bars represent an efficient way to drag material to the inner $\sim$ 100 parsec of galaxies. However, when this material crosses the inner Lindblad resonance (ILR), the inflow is stopped and the gas is redistributed along the ILR ring. Indeed, the presence of lonely bars could not be directly related to an increase in the accretion onto the SMBH and then with the activity in AGNs, this because they are observed with almost the same frequency in both active and non-active galaxies [54]. The presence of additional inner bars or spirals could allow a renewed inflow of material within the ILR. Observational and theoretical studies are being carried out to verify this assumption. Recent hydrodynamic models suggest that spirals induced from strong bars can fuel the SMBH with accretion rates up to 0.03 $M_{\odot}yr^{-1}$ [64], enough to power AGNs and generally above the amounts inferred from bolometric luminosities in nearby active galaxies.

1.2.4 Inflows and Outflows

Not just bars, but non-axisymmetric potentials in general are an efficient way to promote gas inflow towards the inner regions of galaxies [28]. Close encounters and galactic mergers have also been identified as a mechanism capable of driving gas from tens of kiloparsecs down to a few kpc [26, 44], the latter (only major mergers) are likely the only mechanism capable of triggering the most luminous AGNs [105]. Simulations by Hopkins and Quataert (2010) [47] suggest that in gas-rich systems, at scales of 10 to 100 pc, inflows are achieved through a system of gravitational instabilities over a wide range of morphologies such as nuclear spirals, bars, rings, barred rings, clumpy disks and streams.

Different works studying gas kinematics in nearby galaxies [31, 60, 89–91, 101], have search for signatures of gas inflows and/or outflows to/from the nucleus in order to understand the mechanisms responsible for transfering mass from galactic scales down to nuclear scales to feed the SMBH. This is because it is widely accepted that the radiation emitted by an AGN is a result of the accretion on to the SMBH. The searching of this signatures has been motivated (in the last few years) by the finding of Lopes (2007) [95] that there is a marked difference in the dust and gas content of this regions in early-type active galaxies when compared to non-active ones:

while the first always have dusty structures, in the form of spiral and filaments at hundreds of parsecs scales, only 25 per cent of the non-active ones have such structures. This indicates that a reservoir of gas and dust is a necessary condition for the nuclear activity and also suggests that the dusty structures are tracers of feeding channels to the AGN [89, 90]. This fact, along with the enhanced frequency of dusty spirals, supports the hypothesis that nuclear spirals are a mechanism for fueling the SMBH, transporting the gas from kiloparsec scales down to a few tens of parsecs of the nucleus.

On the other hand, accretion onto the SMBH requires removal of angular momentum, which can be achieved through gravitational torques and also via outflows or winds [10], the most powerful of which are produced by the interaction between the ionized gas and the magnetic field [6] reaching velocities of up to 1000 km s^{-1} [38, 85] and outflow rates several times larger than host galaxy star formation rates [103]. Massive AGN-driven outflows have been observed in many objects, from Seyfert galaxies to quasars, at low [66] and high redshifts [70], and could dramatically affect the evolution of galaxies due to the large amount of energy they feedback into the interstellar medium [26]. Radio images showing jets and lobes associated with AGN are a clear evidence that these objects are capable of eject material from their energetic nuclei at relativistic speeds [9].

At the less powerful end, studies of nearby Seyferts show that compact outflows ($\sim$100 pc in extent) with velocities of $\sim$100 km s^{-1} and mass outflow rates of a few solar masses per year are common in low-luminosity AGNs [e.g., 22, 68]. At these low outflow velocities it can be difficult to disentangle if AGNs or host galaxy starburts are responsible for the outflow. A cutoff of 400–500 km s^{-1} is often used [73] to differentiate the two, since that velocity requires $\sim$ 1 keV per particle, something difficult to achieve with stellar processes in large masses of cold molecular gas [29] and, therefore, can only be due to a powerful AGN in the center of the galaxy. For this purpose emission lines of high ionization (also called corona lines) can be used, since they are free of potential star formation contributions, thus providing a direct view of the dynamic forces and structures associated with AGN. These lines are without apparent distinction in AGNs of any kind [81, 84] and have been of great help in supporting the unified model.

Observations of the coronal line region (CLR) show that this region is probably closer to the AGN than the NLR and, therefore, is associated with the outflow component [67]. Murayama & Tanigushi (1998a) [69], based in the [Fe VII] line, proposed that this region comes from the inner wall of the AGN's dusty torus, since Seyferts 1 show CLR emission excess with respect to Seyferts 2, considering the unified model [1]. This means that the radiation of the CLR is anisotropic, so a statistical study of its properties can be used to estimate the angle of vision to the dust torus of several types of Seyfert galaxies and to better fit conical models for the AGN outflow.

To identify low velocity outflows, relatively high spectral resolutions and two - dimensional spectroscopy are required in order to disentangle the different velocity components that may be present: from the galactic disk, and from outflow(s) and/or inflow(s) [90, 102]. Besides, in some special cases these outflows are detected more frequently as redshifted winds, rather than blueshifted, since the light from the ionized regions reach us preferentially from the receding side of the outflow which, for the line-of-sight, is more illuminated by the AGN [e.g., 60]; thus the kinematics can be modeled as a combination of a biconical outflow and a rotating disk coincident with the molecular gas [34, 68].

1.2.5 AGN Feedback

Outflows could be very important for the evolution of galaxies due to the fact that they can be the most efficient way for the interaction between the AGN and its host galaxy, what is called the AGN feedback, affecting the interstellar medium and the star formation. Several works explored whether this process triggers (positive feedback) or extinguishes (negative feedback) the host galaxy star formation [29, 49]. Empirical scaling relations between the masses of the SMBH and the host-galaxy bulge [e.g., 33, 39, see Fig. 1.8], and between the AGN luminosity and molecular outflow velocity [103] or dynamical mass [61], have motivated a deeper study of

this effect.

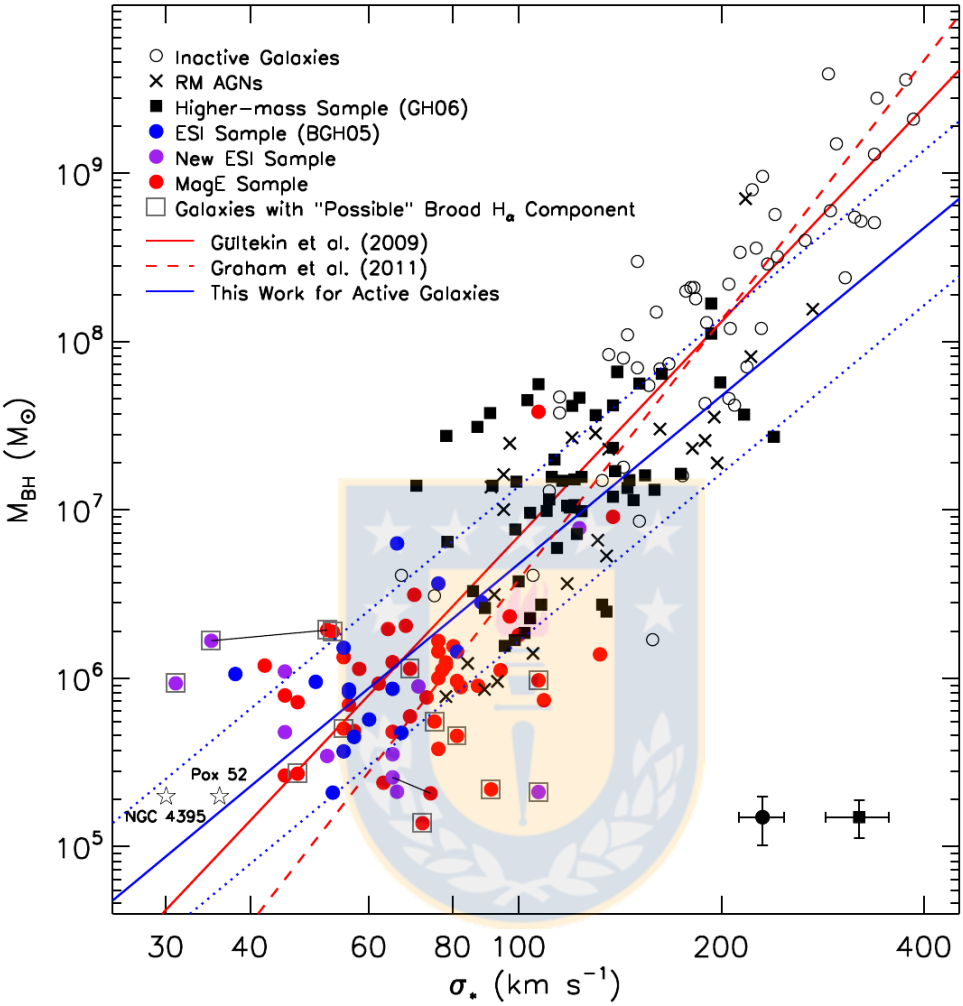

Figure 1.8: A recent calibration of the M-sigma relation, including many low-mass galaxies. They find a lower limit for SMBH mass of 200,000 solar masses within the SDSS spectroscopic sample. From Figure 6 of Xiao et al. (2011) [115].

It can be shown that the growth of the SMBH by accretion in an AGN could have an important effect on its host galaxy: The binding energy of the galaxy bulge of mass M_{gal}, is $E_{gal} \approx M_{gal}\sigma^2$, where σ is the velocity dispersion in the galactic bulge. Considering that the mass of the black hole is related with the mass of the galactic bulge in the form: $M_{BH} \approx 1.4 \times 10^{-3} M_{gal}$ [42, 55], and assuming a mass-to-energy conversion efficiency for the accretion process of 10% [94], so that the energy released by the growth of the black hole is given by $E_{BH} = 0.1 M_{BH} c^2$. The binding energy of the black hole divided by that of the galaxy bulge is: $E_{BH}/E_{gal} \approx 1.4 \times 10^{-4}(c/\sigma)^2$. Since the majority of galaxies have $\sigma < 400$ km s^{-1}, the ratio E_{BH}/E_{gal} usually is greater than 80. Therefore, if a small fraction of this energy can be transfered to the gas, an AGN can have a profound effect on the evolution of its host galaxy.

1.3 Ringed Galaxies

This section is mostly based on the work made by Buta & Combes (1996) [12] and references therein. According to the authors, rings are an interesting aspect of galaxy structure. In figure 1.9, the appearance of some otherwise normal galaxies is dominated by a ring of high contrast. It is possible to observe three main types of optical ring phenomena: nuclear rings, inner rings, and outer rings. These features an be very striking in appearance, as in Figure 1.9b, or be merely part of the spiral pattern, which turns out to be the normal situation (as seen in fig. 1.9a). Although rings appear to be a common aspect of galaxy morphology, the features are hardly discussed at any length in introductory or graduate textbooks and are often treated just as a "detail" of morphology. Yet, ringed galaxies are fundamentally interesting for a variety of reasons, not the least of which is the possible (and almost certain) association of the rings with dynamical orbit resonances. Since the vast majority of ringed galaxies are not violently interacting with other galaxies, it seems certain that rings are mainly a problem of internal dynamics. In fact, it is believe that rings may be a normal phase in the morphological evolution of many galaxies.

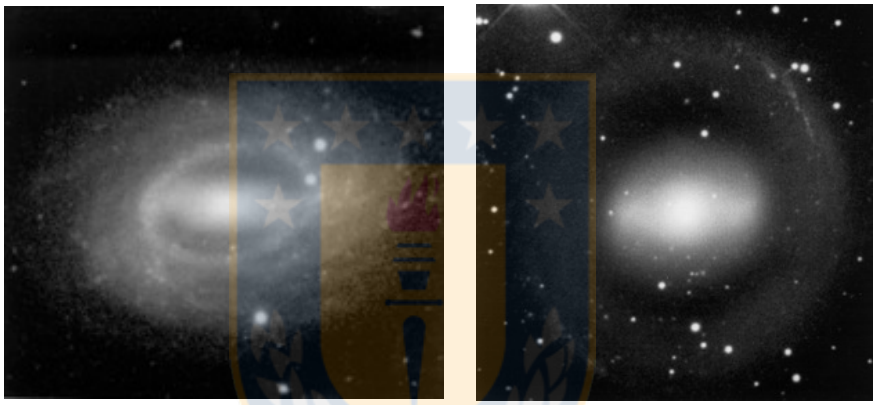

(a) IC 5420, an example of a barred, inner-ringed galaxy

(b) NGC 1543, a pure outer-ringed galaxy.

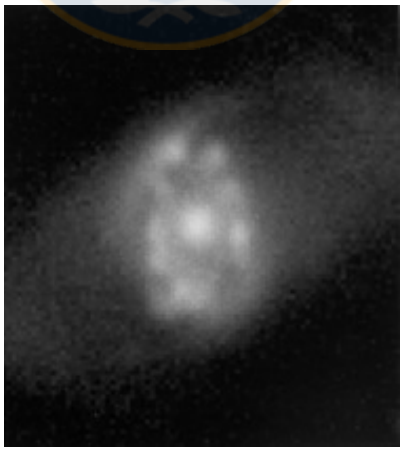

(c) NGC 1300, an example of nuclear ring in an early-to-intermediate type galaxy. From Buta & Combes (1996) [12].

Figure 1.9: Three different examples of ringed galaxies. Images from Buta & Combes (1996) [12].

1.3.1 Inner Rings

The discovery of rings parallels the discovery of spiral structure in the 19th century, because some ring and pseudoring structures in several nearby galaxies were bright enough to have been seen visually with the 1.8-m speculum reflector of Birr Castle Observatory and other telescopes. The accuracy of these early observations was confirmed through photographic observations with the Lick Crossley reflector in 1898-1900 by Keeler (1908) [51]. However, it was Curtis (1918) [20] who first brought attention to a special class of spiral "nebulae" where a ring or pseudoring and a bar were characteristic parts of the structure. The objects Curtis first described are now recognized as "barred spirals" and the near perfect ring as an "inner ring". Although Curtis referred to them as ϕ-type, a term such as θ-type is actually more appropriate since the bar never exceeds the extent of the ring.

1.3.2 Outer Rings

Perrine [78] discovered a second type of ring structure in the southern barred galaxy NGC 1291 that more properly had to be called an “outer ring” or an “external ring”. De Vaucouleurs & Buta (1980b) note that the outer ring of NGC 1291 was already visible on chart 29 of the Franklin-Adams sky charts published in 1910. It is interesting that the outer ring of NGC 7217 is also plainly visible in the photograph in Keeler (1908). In the revised Hubble classification systems described by both Sandage (1961) and de Vaucouleurs (1959a), outer rings are denoted by the symbol (R). De Vaucouleurs commented that such a structure is often observed in lenticulars and early-type spirals but that it is not clearly related to a specific class or family. Later studies (e.g. Kormendy 1979a) have suggested that such rings may be most prevalent in barred galaxies. An example of this type of rings can be seen on figure 1.9b.
As with inner rings, outer rings are closely linked to the spiral pattern, and occasionally the ring is a wrapped pair of spiral arms that nearly close together. In such cases, the ring is referred to as an outer pseudoring and is symbolized by (R’).

1.3.3 Nuclear Rings

The third type of ring structure, the nuclear ring, is the smallest of the three ring types. Some of the first examples were noted by Morgan (1958). He described how some nuclei in spiral and barred galaxies are made up of multiple "hotspots", with type examples being NGC 1808, 3351, 4321, and 5248. Concurrently with this study, Sersic (1958) commented on the existence of an intriguing structure in the center of the SBb galaxy NGC 1097, where a “central knot is surrounded by a chain of condensations forming a single spiral arm.” Burbidge & Burbidge (1960) later observed this object and noted that the nucleus of the galaxy is a segmented annulus consisting of bright areas and probably dust.
Surprisingly, no clear examples of nuclear rings are described in the visual observation notes of W. Parsons and co-workers (Parsons 1926), although some may have been suspected. This may be explained in part by the fact that the rings are more prominent at blue than at visual wavelengths, by their location on the steep background light gradient of the bulge, and that some of the biggest and brightest examples are in the southern hemisphere and not accessible to the latitude of Birr Castle.
The discovery of nuclear rings followed that of the previous two types of ring probably because of strong selection effects against detecting a very small, high surface brightness feature located in a region that is often overexposed on direct photographs. In figure 1.9c it is possible to appreciate the "hotspots" described before.

Chapter 2

About ESO 153-g20

In this work, we present results from integral field spectroscopic observations of the nuclear region of ESO 153-G20, a nearby SBab galaxy harbouring a Seyfert 2 nucleus [RC3: 24, 25]. It is located at a distance of 79.4 ± 5.6 Mpc (from NED[1], derived assuming a redshift of 0.019737 and $H_0 = 73.0$), corresponding to a scale of 385 pc arcsec^{-1} and a heliocentric velocity of 5917 ± 28 km/s [21]. Many extremely different major axis position angles (hereafter PA) have been suggested for this object, from 14° [59], through 125° [96, hereafter 2MASS] to 164.3° [76, ; HYPERLEDA]. This variation is primarily a result of the presence of rings [11, 14] which change the perspective of this object depending on the observation band used. For example, Schmitt and Kinney [88] find $PA_I = 8$ degrees and a PA_B = -50 degrees.

(a) STScI Digitized Sky Survey (DSS) Image of the galaxy.

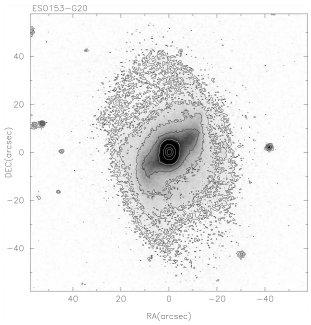

(b) I-band image of ESO 153-g20.

Figure 2.1: Images of ESO 153-g20 from the database. In 2.1a we have the DSS image and in 2.1b, the I-band image obtained from [88]

[1]The NASA/IPAC Extragalactic Database (NED) is operated by the Jet Propulsion Laboratory, California Institute of Technology, under contract with the National Aeronautics and Space Administration.

Listed diameters of ESO 153-G20 vary from 93 to 114 arcsec [RC3; 58, 59, 2MASS], using a reference level of ∼25.0 B-mag arcsec^{-2} in the case of the former three works, and a reference level of 20.0 K-mag arcsec^{-2} in the case of 2MASS. For the minor axis, we found only one determination of 72 arcsec [58] using the same reference level of 25.0 B-mag arcsec^{-2}. An ellipticity between 0.37 and 0.40 has also been determined by the same authors.

The rings in this galaxy have been relatively well characterized. Buta [11], Buta and Crocker [14] determine that this galaxy is a classical example of a "2+2" spiral arm multiplicity, i.e., two main arms and two secondary ones. It shows a very open inner pseudoring (rs) around a prominent bar and is one of the best cases of Type I Schwarz outer pseudoring (R'$_1$) according to Buta and Crocker [13].
In a Hubble Space Telescope (HST) survey of extended [O III]λ5007 emission in Seyferts, [87] found that the bulk of the emission line region is extended along PA=-100° and comes from the inner 1 arcsec (see Fig. 2.2). They also find some diffuse emission in a region of ∼1.85 × 2.65 arcsec^2 around the nucleus, with a major axis at PA=-10°.

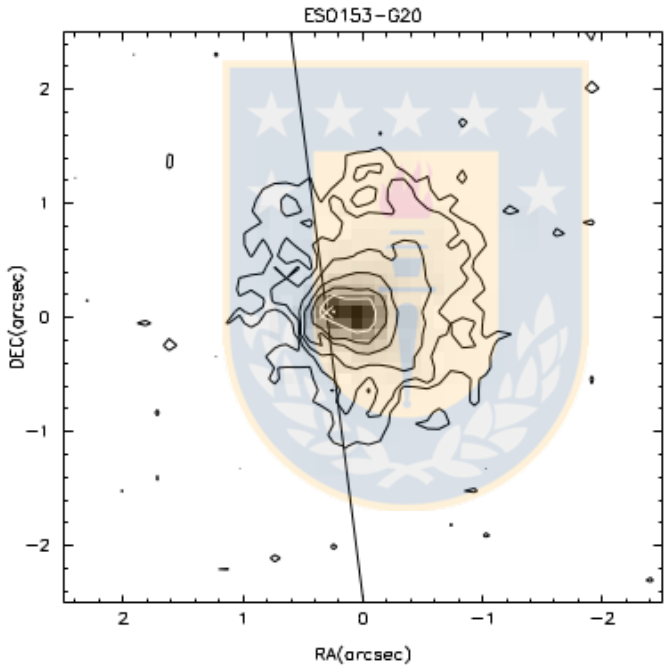

Figure 2.2: From fig. 5 of Schmitt et al. (2003) [87]. [O III] continuum-subtracted image of ESO 153-G20. The contours start at the 3σ level above the background and increase in powers of 2 times 3σ (3$\sigma \times 2^n$). The position of the nucleus, measured in the continuum images, is plotted as a white cross. The position-angle of the host galaxy major axis is shown as a solid line crossing the figure through the nucleus. North is up, and east is to the left.

The more recent discovery in this galaxy was the supernova 2012U (Bock et al. 2012) [7], a type-Ia supernova located 8 arcsec east and 2 arcsec south of the nucleus. Fig. 2.3 shows the SN when it was first discovered.

Figure 2.3: Image of the supernova 2012U when it was first discovered and it was just a SN candidate.

Chapter 3

Gas and Stellar kinematics in ESO 153-g20

3.1 Observations and Data Reduction

The observations were obtained with the Integral Field Unit of the Gemini Multi-Object Spectrograph (GMOS-IFU) at the Gemini South telescope on the night of 2014 October 29 as part of project GS-2014B-Q-20 (P.I. Nagar). The observations were obtained in 'one-slit' mode and consisted of two adjacent IFU fields, covering a field of view (FOV) of 3.5 $\times$ 5 arcsec^2 each, and resulting in a total coverage of 3.6 $\times$ 4.9 arcsec^2 around the nucleus. Two exposures of 900 seconds each were obtained for each field, slightly shifted spatially and in wavelength coverage, in order to correct for detector defects after combination of the frames. The seeing during the observation was $\sim$0.65 arcsec, as listed in the observation log, and confirmed by measuring the full width at half-maximum (FWHM) of the profiles of four stars in the science acquisition image. This corresponds to a spatial resolution of $\sim$ 250 pc at the distance of the galaxy.

The selected wavelength range was 4110-7280 Å, in order to cover the Hβ, [O III] $\lambda\lambda$4959,5007; Hα+[N II] $\lambda\lambda$6549,6583 and [S II] $\lambda\lambda$6717,6731 emission lines, observed with the grating GMOS B600_G5323 (set to central wavelength of either λ 5700 Å or λ 5750 Å) at a spectral resolution of R $\approx$ 3550 with $\sim$0.51 Å per pixel and an instrumental dispersion (σ_{inst}) of $\approx$ 36 km s^{-1}, as measured from the arc spectra used for wavelength calibration.

Data reduction was performed using specific tasks developed for GMOS data in the *gemini.gmos* package as well as generic tasks in *PyRAF*[1]. The reduction process included bias subtraction, bad pixel masking, flat-fielding, trimming, wavelength calibration, sky subtraction, relative flux calibration, building of the data cubes at a sampling of 0.1 $\times$ 0.1 arcsec^2, and finally the alignment and combination of the four data cubes using the *PyFU*[2] package. We also performed cosmic ray rejection using the Laplacian Cosmic Ray Identification (L.A.Cosmic) written by van Dokkum et al. [110].

Flux calibration was performed using the spectroscopic standard star LTT 2415 (V=12.21) for which fluxes are tabulated every 50 Å [40, 41]. It was observed in a 600 s exposure on the night of October 11, 2014 with the same instrument setup as the galaxy. The flux calibration step applies by default an arbitrary scaling of 10^{15} in order to avoid later numerical errors. This factor was considered to get true flux units in our analysis.

[1] PyRAF is a product of the Space Telescope Science Institute, which is operated by AURA for NASA.

[2] Version 0.9 of the PyFU 3D data manipulation package was contributed by James Turner through the Gemini Data Reduction User Forum.

Sky subtraction was performed using spectra from the "Sky" IFU. In Fig. 3.1 we note a residual Telluric absorption at ∼6870Å (see spectrum at position (1)) that affects the [S II]λ6731 emission line. In order to correct this feature, we create a pseudo-spectrum of the standard star, using the absolute magnitudes on the V, R, I, J, H, K bands and the *imexpr* task from *IRAF*[3]. The observed spectrum of the standard star is divided by this pseudo-spectrum in order to obtain a "flat" spectrum which was used to correct for Telluric absorption in each spectrum of the data cube. The result of this process can be observed in the last two panels of fig. 3.1. We note that the science and flux calibrator exposures were taken on different nights, and thus the Telluric subtraction is not optimal. This does not change any of our principal science results as this absorption only affects a small region close to the [SII] lines.

3.2 Results

Figure 3.1 presents an overview of our target galaxy and observations. The upper left panel shows the Gemini GMOS acquisition image of ESO153-G20. The upper right panel shows an image of the inner 8×8 arcsec^2 of the galaxy obtained with the Wide-Field Planetary Camera 2 (WFPC2) through the filter F547M aboard the *Hubble Space Telescope (HST)*. The middle left panel presents a 'structure' map of the same FOV as the WFPC2 image, where the rectangle shows the FOV of our Gemini GMOS observations. This structure mapwas obtained following the process detailed in Pogge and Martini [80], which uses the HST image and a PSF for convolution. In this case, we used synthetic PSFs created with the Tiny Tim software (Krist et al. [57]). In the structure map we clearly see more dust obscuration to the NE direction, and thus conclude that the near side of the galaxy disk is to the NE. The red circles plotted on each side of the galaxy will be discussed in Chapter 4; these correspond to the apertures towards which we posit a visible ionization cone (SW) and its corresponding obscured cone (NE). In the middle right panel we show the stellar continuum image from Gemini/GMOS-IFU, obtained by integrating the flux within a line-free spectral window from λ5400 Å to λ5800 Å. The solid line represents the kinematic major axis of the galaxy (PA=10.5°), obtained from our analysis of the stellar kinematics (see section 3.2.1), and the dashed line represents the minor axis.

In the lower panel of Fig. 3.1, we present three spectra from the locations marked as 1 (nucleus), 2 (intermediate region) and 3 (boundary region) in the IFU image and extracted using an aperture diameter of 0.4 arcsec (∼ 154 pc). The nucleus of the galaxy was adopted as the position of the stellar kinematic center. We clearly detect strong emission lines - Hβ, [O III] $\lambda\lambda$4959,5007; Hα+[N II] $\lambda\lambda$6549,6583 and [S II] $\lambda\lambda$6717,6731 - in all the spectra. All permitted lines show only 'narrow components', consistent with the classification of ESO 153-G20 as a Seyfert 2 galaxy.

3.2.1 Stellar kinematics

In order to measure the stellar kinematics, we employed the Penalized Pixel Fitting technique (pPXF) [15, 17] using as template spectra the MILES Stellar Library [30, 86, 111]. These models have a spectral resolution of 2.5 Å (FWHM), or $\sigma_{inst} \sim 64$ km s^{-1}, and cover the range 3525-7500 Å. The final dispersion maps obtained were corrected, in quadrature, for both the mismatch in the spectral resolution of the science spectra and templates, and the intrinsic spectral resolution of the science spectra. To ensure the reliability of the stellar kinematic measurements, the final datacube was spatially binned using the Voronoi binning method [16], creating bins with a minimum signal-to-noise ratio (S/N) of 25 per bin.
Before running pPXF, we first identified and masked out the spectral regions contaminated by emission lines, this included the emission lines mentioned in section 3.1 along with Hδ, Hγ, He II λ4685, [N I]$\lambda\lambda$5198,5200 and [O I] $\lambda\lambda$6300,6363 emission lines. The bottom panels of Fig. 3.1 show example results from pPXF and the respective residual and emission-line-only spectra.

[3]IRAF is distributed by the National Optical Astronomy Observatories, which are operated by the Association of Universities for Research in Astronomy, Inc., under cooperative agreement with the National Science Foundation.

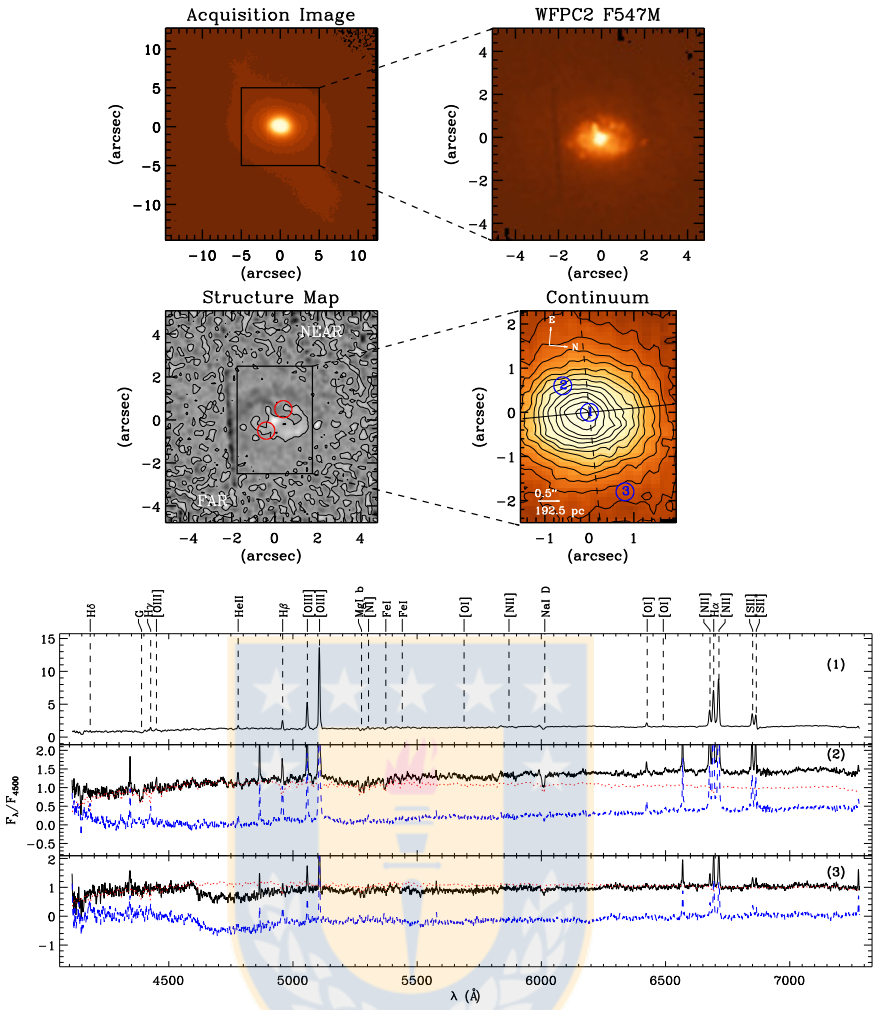

Figure 3.1: Acquisition image, HST image, structure map and continuum image of ESO 153-g20 plus some spectra. *Top left:* acquisition image from Gemini-GMOS. *Top right:* WFPC2 image of the nuclear region marked on the acquisition image. *Middle left:* 'structure' map showing the FOV of the observation. *Middle right:* stellar continuum image derived from the IFU datacube. *Bottom:* observed-frame spectra (black continuum line) corresponding to the regions marked as (1), (2) and (3) in the continuum image. For regions (2) and (3) we also show the best-fit stellar spectrum derived by *pPXF* (red dotted line) and the residual (observed minus stellar) spectrum (blue dashed line). Image from the author.

The stellar velocity field (v_*) derived from pPXF is shown in the left panel of Fig. 3.2. There is a clear rotation pattern reaching projected velocities of ≈ 96 km s^{-1} within our FOV. The line of nodes is oriented close to the North-South direction, with the N side receding and the S side approaching. While the major axis is along the shorter side of our FOV we are still able to get reliable results for the kinematics. The stellar velocity dispersion (σ_*), shown in the rightest panel, varies between 76 km s^{-1} and 188 km s^{-1} across the FOV.

We have fitted a rotation model to the stellar velocity field, after obtaining the best-fit systemic velocity of the galaxy ($V_s \approx 5907.4$ km s^{-1}) and the PA of the kinematic major axis (PA=10.5°) using both *Kinemetry* and *Fit kinematic PA* [56] IDL routines. For this purpose, we assumed the kinematical centre as the zero velocity point of the stellar velocity field.

Assuming a spherical potential and circular orbits in a plane, the observed radial velocity at a position (R, ψ) in the plane of the sky is given by [5]:

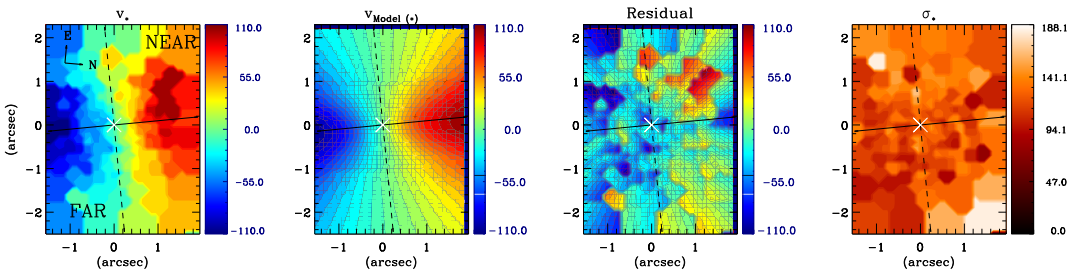

Figure 3.2: From left to right: Stellar centroid velocity field ($\mathrm{km\,s^{-1}}$), best-fit Bertola rotation model, residual (centroid velocity field - model) and stellar velocity dispersion ($\mathrm{km\,s^{-1}}$). The continuum (dashed) lines mark the position of the kinematic major (minor) axis and the crosses mark the stellar kinematic center. Image from the author.

$$V = V_s + \frac{AR\cos(\psi-\psi_0)\sin(\theta)\cos^p\theta}{\{R^2[\sin^2(\psi-\psi_0)+\cos^2\theta\cos^2(\psi-\psi_0)]+c^2\cos^2\theta\}^{p/2}} \tag{3.1}$$

where θ is the inclination of the disc (with $\theta = 0$ for a face-on disc), ψ_0 is the position angle of the line of nodes, V_s is the systemic velocity, R is the radius and A, c, and p are parameters of the model.

The resulting parameters A, c and p of the fit to the stellar field are shown on the second column of table 3.1. The second and third columns of Fig. 3.2 show the best-fit stellar rotation model and the velocity residual.

Table 3.1: Parameters of the best-fit rotation model for stars and [N II]. Table from the author.

Parameter	Stars	[N II]	[N II] "eye" fit
A ($\mathrm{km\,s^{-1}}$)	144.9	264.8	280
c (arcsec)	1.22	3.0	1.2
p	1.0	1.0	1.0
i (degrees)	51.32	51.32	46.0
PA (degrees)	10.5	10.5	10.5

Notes: Column 1 corresponds to the parameter name; Column 2 shows the best-fit parameter value for the stellar velocity field; Column 3 is the same as Column 2 but for the [N II] velocity field; and Column 4 shows the values for the [N II] "by eye" fit.

3.2.2 Gas Kinematics

Single Gaussian Fit

To obtain line emission fluxes, centroid velocities and velocity dispersions, we used the *Profit* IDL routine [83] to fit the strong emission lines with a single Gaussian or Gauss-Hermite profile. In this process it was immediately obvious that in some regions a double Gaussian fit should be necessary. Nevertheless it is instructive to first present the results from the single Gaussian fit. In Fig. 3.3 we present the integrated flux distributions, velocity fields and dispersion maps of the [O III] λ5007 Å, Hα, Hβ, [N II] λ6583 Å and [S II] λ6716 Å emission lines.

The emission line fluxes show higher values within a region with radius ∼1 arcsec (385 pc), centered about 0.25 arcsec to the SW of the stellar kinematic center. The flux distribution

of the [O III] emission line appears mainly axisymmetric but at fainter fluxes it appears to be extended along PA≈110°, close to the value reported by Schmitt et al. [87] using HST imaging. In the case of Hα and Hβ, the distributions appear more symmetric with respect to the nucleus, reaching values of 0.9 and 0.2 10^{-15} $erg\ cm^{-2}\ s^{-1}$ respectively. These distributions also seem to be extended to the N direction. Both [N II] and [S II] distributions seems to be an intermediate between [O III] and Hα, being slightly axisymmetric and showing a little elongation to the N.

The centroid velocity maps for Hα, Hβ, [N II] and [S II] (second line of Fig. 3.3) show signatures consistent with rotation in a disk, reaching amplitudes of ~ 200 km s^{-1}, but also showing some distortions. These distortions are particularly notorious in the case of Hα, which shows an "S" shaped velocity pattern characteristic of barred disk galaxies. On the other hand, the [O III] emission line shows significantly lower velocities, reaching values of only $\sim$30 km s^{-1} in the inner 1.5 arcsec. To better visualize the large difference in the [O III] kinematics Fig. 3.4 plots the change of velocity with radius along the (stellar) kinematic major axis, i.e. the rotation curve, of all strong emission lines. Here the Hα, [N II] and [S II] emission lines show a clear rotation signature while the [O III] emission line is mostly close to zero velocity.

We fitted a Bertola rotation model to the [N II] emission line velocity map, following the same procedure as for the stellar field 3.2.1. The parameters A, c and p were free while the inclination and major axis PA were fixed to the values determined from the stellar velocity field best-fit. Using the results of the best-fit to the emission line as a starting point, we changed all parameters in order to obtain a model which best fit (by "eye") the P-V diagrams presented in Sect. 3.2.2. This gave significantly different results since, as mentioned above, the observed gas kinematics appears to show multiple velocity components, so that the velocity field from the single Gaussian fit does not only reflect the rotating gas component. The parameter values of these two Bertola fits to the emission line kinematics are listed on the third and fourth columns of Table 3.1.

Velocity dispersion maps of the emission lines, after correction of the instrumental resolution (σ_{inst} ≈36 km s^{-1}) are shown in the third line of figure 3.3. The mean dispersion value seen over all emission lines is $\sim$ 90 km s^{-1}.

Figure 3.5 shows the the rotation models obtained for the stellar and [N II] emission line along with the gas velocity residuals (observed - modeled) fields. Both visually, and comparing the rms in the residuals, it is clear that the emission lines show velocity fields more in agreement with the [N II], rather than stellar, rotation model.

Figure 3.6 presents maps of the estimated electron density and the [N II]/Hα, [O III]/Hβ, Hα/Hβ, [S II]6716/6730 line ratios. The electron density was obtained from the [S II] line ratio, assuming an electron temperature of 10,000 K [75]; it is as high as 800 cm^{-3} at the nucleus and decreases to $\sim$ 400 cm^{-3} at 1 arcsec from the nucleus.

The [N II]/Hα line ratio has values between 1.0-1.5 within the inner 1 arcsec while Hα/Hβ reaches values between 3.9 to 5.2 within the same region. The [O III]/Hβ line ratio varies between 4.6-11.0 in the inner 1 arcsec, with a value of 8.4 in the nucleus. These ratios are typical of AGNs rather than star-forming (HII region) galaxies [50, 52].

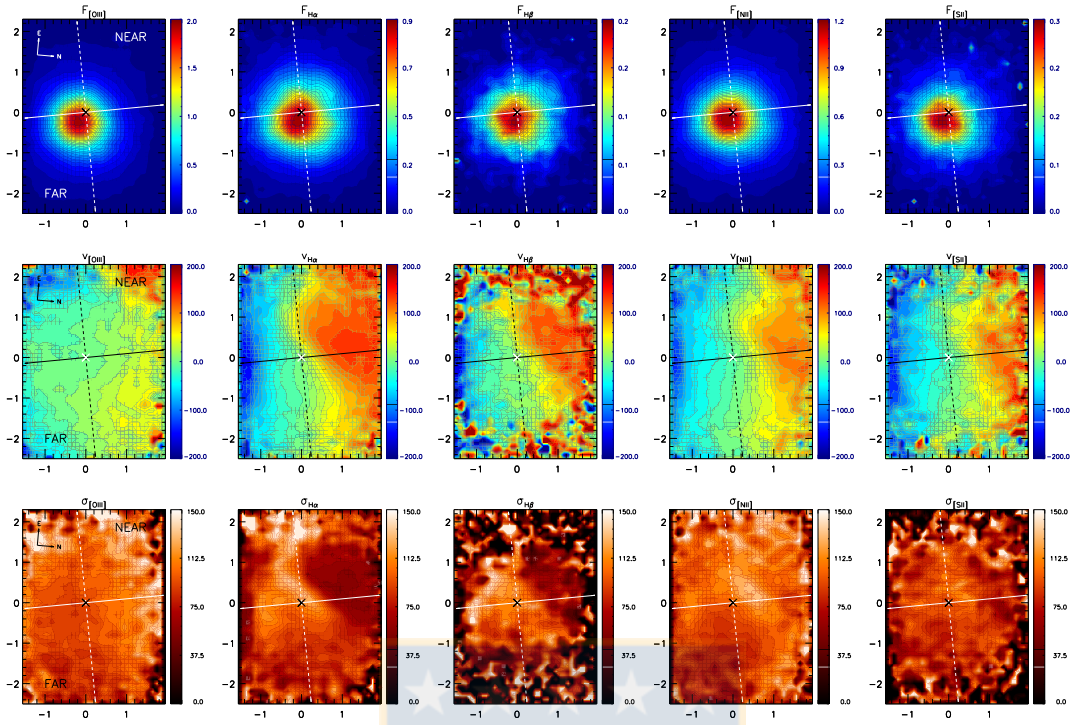

Figure 3.3: From top to bottom: Maps of the integrated fluxes (10^{-15} $erg\ cm^{-2}\ s^{-1}$ per pixel), centroid velocities ($\mathrm{km\,s^{-1}}$) and velocity dispersions ($\mathrm{km\,s^{-1}}$) derived from the single Gaussian fit to the [O III], Hα, Hβ, [N II] and [S II] emission lines. Each panel follows the color bar on its right and the axes (in arcsec) are relative to the stellar kinematic center, indicated by the intersection of the solid and dashed lines on each map. The solid (dashed) line indicates the major (minor) axis. The near and far sides of the disk are indicated on the panels in the leftmost column. The zero velocity corresponds to a systemic velocity of 5907.4 $\mathrm{km\,s^{-1}}$. Image from the author.

Position-Velocity Diagrams and Line Profiles

We made position-velocity diagrams for the three strongest emission lines - [O III], Hα and [N II] - in order to better constrain their kinematics. Our analysis used P-V diagrams, centered on the stellar kinematic center and systemic velocity derived from the best-fit Bertola model to the stellar field, along 18 different PAs spaced by 10°. Figure 3.7 shows the most relevant of these P-V diagrams, including those along the major and minor axes. For a direct comparison, we also overplot the velocities indicated by the single-Gaussian fit to the respective emission line, the best-fit model to the stellar velocity field and the "by eye" fit to the [N II] (which was obtained by visual fitting to these P-V diagrams), and the 'best' bar perturbation model (see Chapter 4 for details on this latter).

It is clear that the velocities from the single Gaussian fit are not very representative of the rotating component in the case of Hα and [N II], specially on the blueshifted side, where the presence of a second lower velocity component is clearly seen. The [N II] "by eye" model, as mentioned in section 3.2.2 is the one which best represents the velocities seen in the Hα and [N II] emission lines in most PAs, though in some PAs it predicts velocities lower that observed on the redshifted side (NE side of the galaxy). In the case of [O III], the P-V diagrams are completely different: there is some small agreement with the predictions of the [N II] model at the faintest contours, but the strongest emission comes from gas with velocities very close to systemic at all PAs and all distances from the nucleus.

To complement the P-V diagrams, in Fig. 3.8 we show normalized spectra of the [O III],

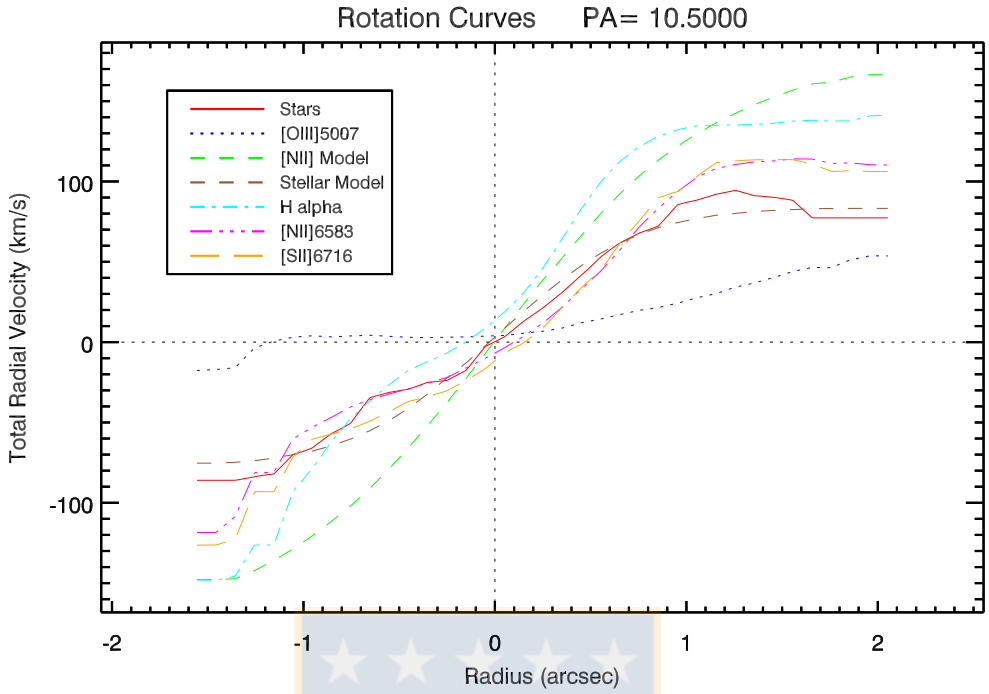

Figure 3.4: Radial velocity 'rotation curves' along the kinematic major axis (PA = 10.5) for the stellar velocity field and the strongest emission lines, following the legend in the top left. For emission lines the velocities are those obtained by the single Gaussian fit. For reference, the best-fit Bertola stellar rotation model and [N II] rotation model are also shown. Image from the author.

Hα, [N II] and [S II] emission lines, extracted from several 0.2 arcsec radius apertures distributed over our FOV. These spectra have been continuum subtracted using the *continuum* task from *IRAF*. Many apertures show two velocity components, but it is easy to appreciate the difficulty of separating these two components since the width of the non-rotating component is similar to the total velocity variation in our FOV in the rotating component. It is easy to determine that the [O III] profile (continuum line) is centered at zero velocity in all apertures, showing slight wings or a small rotation component in agreement with the model prediction in some of the apertures from the right side. Its mean Full Width at 10% is ~ 490 km s^{-1}considering the ones with high S/N. The apertures located in the major axis, and close to it, show that Hα (dot-dashed line) have two components, or one with a slight wing: one component clearly at zero velocity, in agreement with [O III], and the other close to the predicted velocity from the model. The two apertures close to the minor axis show profiles with almost the same behaviour than [O III]. The one to the NE shows the rotating component in Hα, which corresponds to the redshifted location in the velocity maps. The [N II] and [S II] lines show, in all apertures, a behavior intermediate between Hα and [O III], tracing both the rotation and the zero velocity component.

As mentioned previously, the coincidence between the width of the non-rotating component and the total velocity variation in the rotating one doesn't allowed us to perform double Gaussian fits to the Hα and [N II] lines in all the apertures, thus we chose the five apertures where both components can be easily separated in velocity and performed a double Gaussian fit to the Hα profile, since we are using this results in chapter 4 to estimate the gas mass and mass outflow rate. From these fits we obtain a mean dispersion ($\bar{\sigma}$) of ~ 120 km s^{-1} for the non-rotating component, and for the rotating one, a value of $\bar{\sigma} \sim 60$ km s^{-1} was obtained.

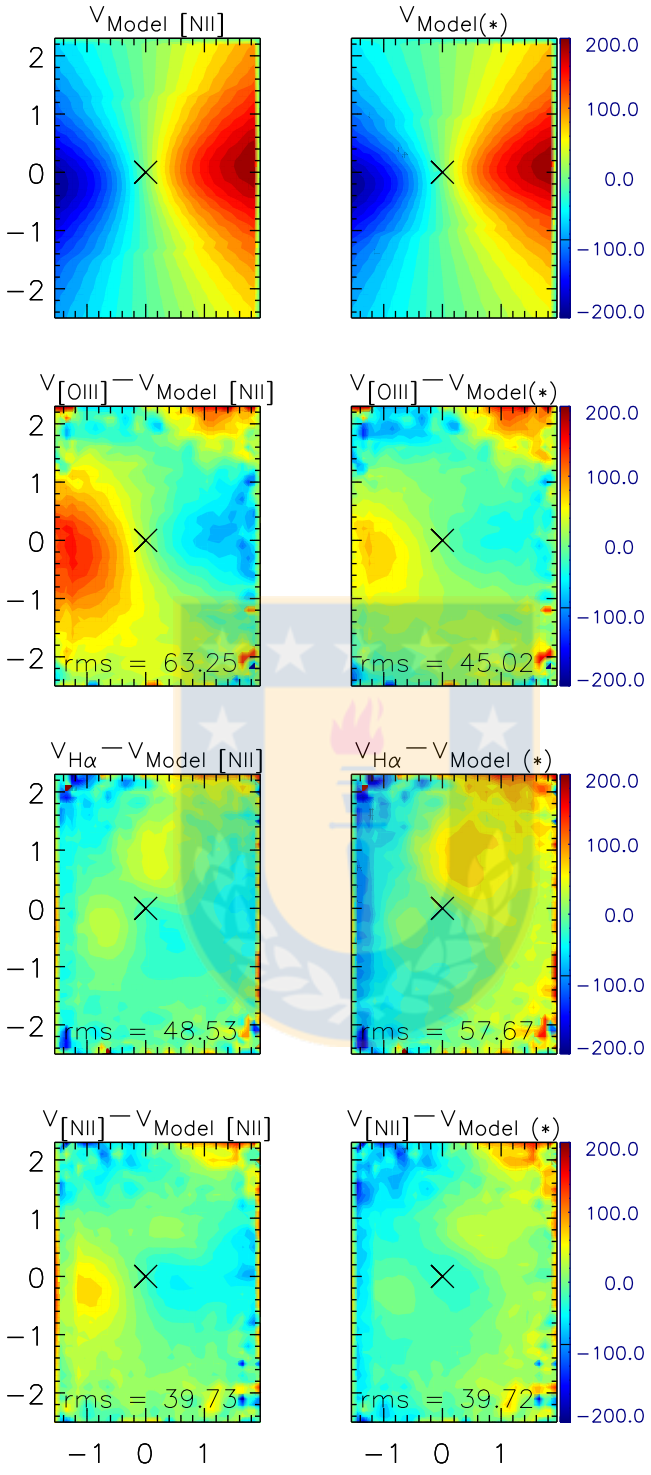

Figure 3.5: The best-fit Bertola rotation model for the [N II] and stellar velocity fields and the velocity residual fields for the [O III], Hα and [N II] emission lines. The stellar kinematic center is marked by a black cross and axes are in arcseconds. Image from the author.

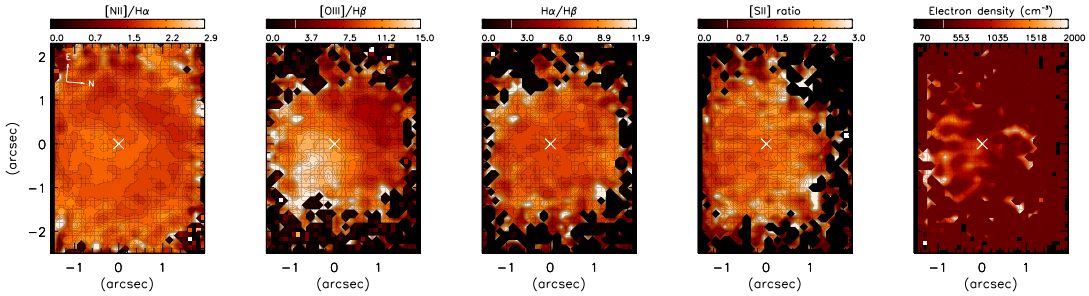

Figure 3.6: Maps of the line ratios [N II]/Hα, [O III]/Hβ, Hα/Hβ, [S II]6716/[S II]6730 and the estimated electron density (cm^{-3}). Each panel follows the color bar on top and the white cross marks the stellar kinematic center. Image from the author.

Double Gaussian Fit

As clearly demonstrated in the previous sections, a second velocity component is often observed in some of the emission lines. We performed double Gaussian fits to the [O III], Hα and [N II] emission lines as they have the highest signal to noise ratio. As discussed in the previous section, it is difficult to attempt a 'blind' two component fit as the apparently non-rotating component has a dispersion which is similar to the total velocity swing of the rotating component over the FOV. We were thus forced to use the following relatively tight constraints: the rotating component was constrained to lie within ± 10 km s^{-1} of the [N II] "by eye" rotation model and the second component was forced to lie within ± 10 km s^{-1} of systemic. Due to the "S" shaped distribution seen in the velocity field derived from the single component fit and the excessive redshift (compared to the model) observed NE direction, the fit in this region failed. To solve this we tried to: (a) relax the allowable velocity shifts from the rotational model, (b) used the peak values of the data as reference instead of the model, i.e. the velocity of Hα as obtained from its peak position; and (c) used the velocity of the [O III] as the first guess for the non-rotating component of Hα and [N II]. For cases (a) and (b) we obtained a rotating component in Hα and [N II] whose velocities are similar to those obtained with the single Gaussian fit, with excessive redshifts to the NE in the non-rotating component. Case (c) gives the most physical and meaningful results and is thus the case we analyzed more deeply.

The flux distributions obtained from this two component fit show, in the case of the [O III] emission line, that the non-rotating component is brighter than the rotating one (a peak value of $1.8{\times}10^{-15}$ vs a peak value of $0.7{\times}10^{-15}$), which is in agreement with what we observe in the line profiles. The flux distribution of the non-rotating component appears symmetric, with the peak flux located ∼0.25 arcsec to the SW from the stellar kinematic center. In the case of Hα, both velocity components follow a similar distribution and have similar intensities, but the rotating component shows a higher extension to the NE direction (the near side) being consistent with gas rotating on the disk of the galaxy. The peak is located slightly to the SW. The [N II] line profiles (Fig. 3.8) are intermediate between those of [O III] and Hα, thus the flux distributions observed for both components appear to be very symmetric with a slightly elongation to the NE and a peak value of $\approx 0.6 \times 10^{-15}$ erg cm^{-2} s^{-1} located slightly to the SW. In figure 3.9, we plot the flux ratio of the rotating component to the zero velocity component for [O III] and Hα. In both cases, the greatest values (up to 6.0 in Hα) are located to the N side of the galaxy.

In the velocity fields of the two component fit (not shown), we recover the rotating pattern seen in the single Gaussian fit in Hα (including the "S" shape), but now with amplitudes of the order of 100 km s^{-1} and a more symmetric distribution. In the case of the [O III], the rotating component is mostly observed to the North with values close to 100 km s^{-1} while to the South, velocity amplitudes of just $\sim$ 50 km s^{-1} are reached; though this asymmetry is likely due to the complexity of separating the two components. For the [N II] emission line, the rotating component reaches amplitudes of the order of $\sim$ 90 km s^{-1}. The non-rotating component, in all

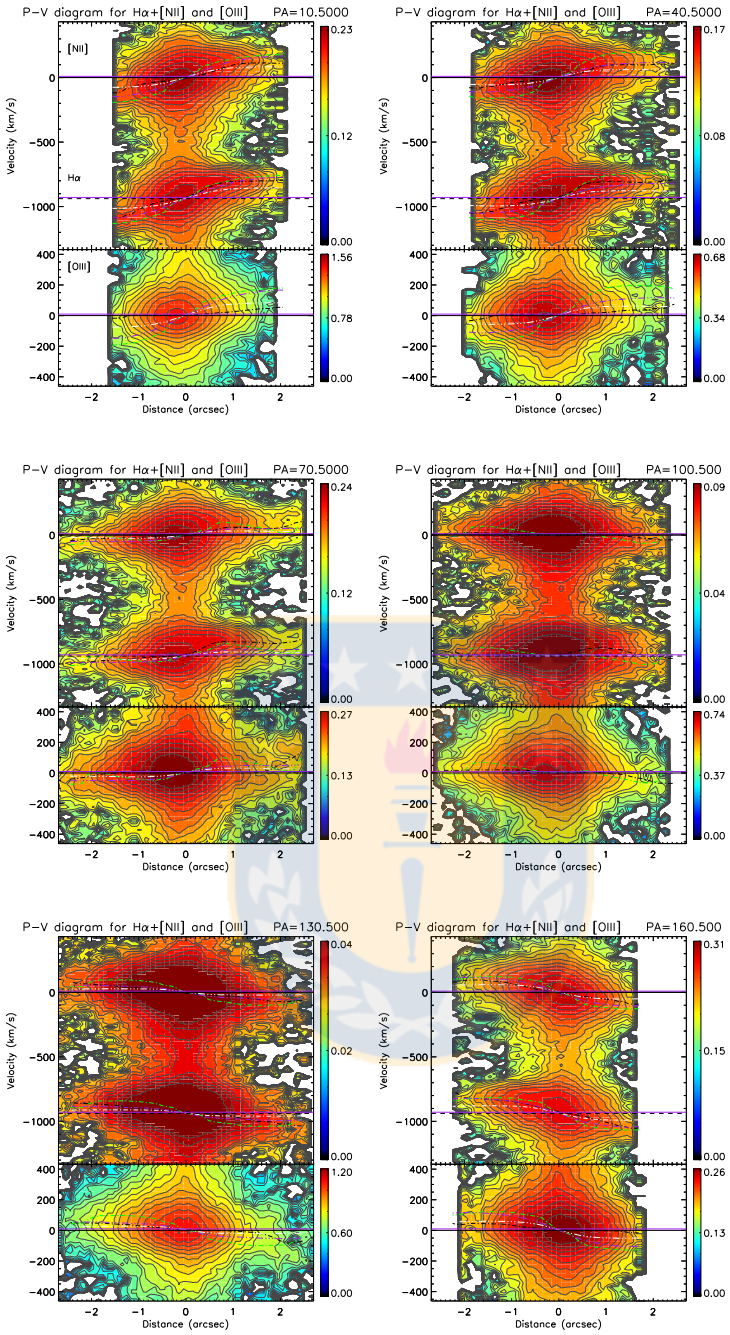

Figure 3.7: Position-Velocity Diagrams of the strongest emission lines: Hα+[N II] and [O III]. The PA of the 'slit' is indicated at the top of each set of panels (the major axis is at PA=10.5°). The black dashed lines show the velocities obtained from the single Gaussian fit, the green dashed line represents the best bar perturbation model (see Chapter 4), the purple dashed line corresponds to the [N II] "by-eye" rotation model and the white dashed line is the stellar rotation model. The color bars on the right of each panel have units of 10^{-15} $erg\ cm^{-2}\ s^{-1}$ per pixel. Image from the author.

emission lines, shows velocity dispersions of the order of $\sim$200 km s^{-1} to the SW, which we will

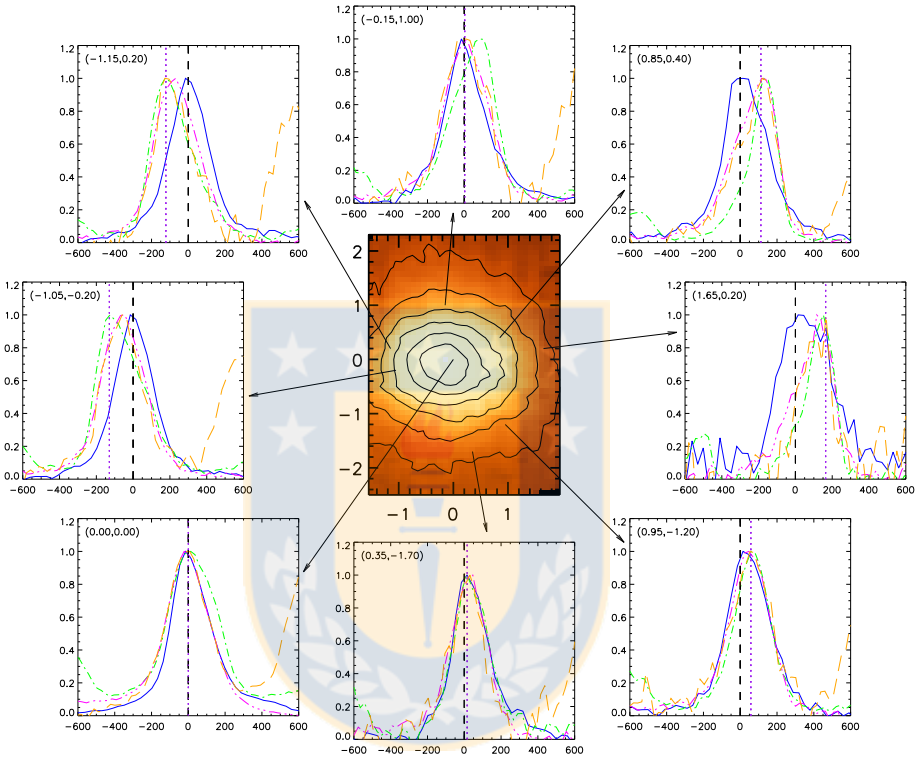

Figure 3.8: Normalized spectra of the [O III], Hα, [N II] and [S II] emission lines (in blue, green, magenta and orange respectively; see text for details) in several 0.2 arcsec radius apertures distributed across the FOV. The aperture position is indicated both in the top left of each panel (as RA and Dec offsets, in arcsec, from the nuclear position) and also on the stellar continuum image at the center. In each panel the vertical black dashed line represents the systemic velocity of the galaxy and the vertical purple dotted line corresponds to the velocity predicted from the [N II] "by eye" rotation model. Spectra are continuum subtracted using the *continuum* task from *IRAF*. Image from the author.

later argue to be due to an ionization cone. In the opposite direction (NE) low velocity dispersions (close to 50 $\mathrm{km\,s^{-1}}$) are seen. Thus overall the second, high dispersion velocity component centered on zero velocity is primarily detected to the SW, while most of the emission line gas to the NE is rotating.

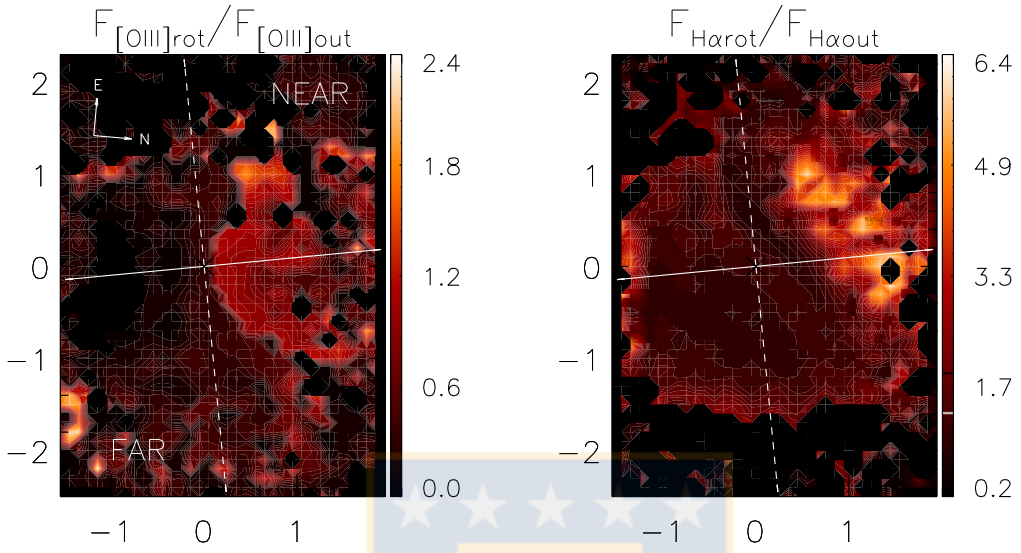

Figure 3.9: The ratio of total flux in the rotating component to total flux in the non-rotating, zero-velocity, component for the two component fit to the [O III] and Hα emission lines. Rotating gas dominates to the NE, and the zero velocity component dominates to the SW. Image from the author.

3.2.3 The Black Hole Mass and Accretion Rate

There is no direct black hole mass measurement for ESO153-G20. We thus use the relationship of [39] to estimate the black hole mass via the central velocity dispersion:

$$\frac{M_{BH}}{10^8\,M_\odot} = (1.312 \pm 0.08) \times \left(\frac{\sigma}{200\ km\ s^{-1}}\right)^{4.24\pm0.41} \tag{3.2}$$

Using the summed spectrum of our datacube and pPXF we find that the stellar velocity dispersion is 190 $\mathrm{km\,s^{-1}}$, which implies a black hole mass of $M_{BH} \approx (1.1 \pm 0.09) \times 10^8\,\mathrm{M_\odot}$ using equation (3.2).

We also estimated the accretion rate onto the black hole using:

$$\dot{M}_{acc} = \frac{L_{bol}}{c^2\eta} \tag{3.3}$$

where η is the conversion efficiency of the rest mass energy of the accreted material into radiation, typically assumed to be $\eta = 0.1$ for Seyfert galaxies [35], and L_{bol} is the bolometric luminosity of our galaxy. We follow Dumas et al. [27] in using $L_{bol} \approx 90 \times L_{[O\,iii]}$. The total [O III] luminosity in our FOV is $L_{[O\,iii]} = 3.5 \times 10^{41}$ $\mathrm{erg\,s^{-1}}$, and thus $L_{bol} \approx 3.14 \times 10^{43}$ $\mathrm{erg\,s^{-1}}$. Substituting these values in equation (3.3) we estimate a mass accretion rate of $5.5 \times 10^{-3}\,\mathrm{M_\odot\ yr^{-1}}$.

Chapter 4

Discussion

We have presented high resolution stellar and ionized gas kiematics in the central kpc of ESO153-G20. Using single and double component Gaussian fits, P-V diagrams, and spectra over selected apertures, we have argued that two velocity components of ionized gas coexist in the central kpc. One component rotates in (mostly) the same sense as the stars. This rotating gas component is clearly seen in all emission lines except [O III] where the two component fit is required to tease out the weak rotating component.

The second component has a relatively large (up to 240 $\mathrm{km\,s^{-1}}$) dispersion and is centered on close to the systemic velocity of the galaxy. While this component is seen in all emission lines, it is strongest in the [O III] line. Further it is present mainly, perhaps only, in a compact region 0.25 arcsec to the SE of the nucleus. A 2D-Gaussian fit to the flux distribution of the non-rotating component in all emission lines gives a mean, almost circular, extent of 1.4 arcsec FWHM. Deconvolving the seeing FWHM ($\sim$ 0.65 arcsec), this implies an intrinsic extent of $\sim$1.2 arsec. The ionization state of the gas to the SW of the nucleus, i.e. spatially coincident with this second component is high, and the line ratios (e.g., [O III]/H$\beta > 10$, see Fig. 3.6) are AGN-like. For all these reasons we interpret this second zero-velocity component as an ionization cone to the SW of the nucleus. Arguments against an origin in an off-nuclear starburst are presented below. Since the second component is centered on systemic velocity, the ionization cone would have its axis along the plane of the sky. The spread of velocities seen, $\pm$240 $\mathrm{km\,s^{-1}}$ would then imply that the illuminated gas is outflowing with velocity $\sim$240 $\mathrm{km\,s^{-1}}$and projection effects and/or acceleration or deceleration along the 1.4 arcsec extent creates the observed spread in observed radial velocities. The locations of the posited ionization cone to the SW and the equivalent position to the NE where we would expect the counter-cone are marked with red circles in the structure map (Fig. 3.1). Clearly the predicted location of the counter-cone is coincident with a strong dust lane seen on the near side of the galaxy disk. Extinction due to this dust lane would explain the lack of detection of the counter-cone. Dust in the nucleus would also explain the offset between the kinematic nucleus and the radius at which the SW ionization cone is first detected ($\sim$ 96 pc). To best obscure the counter-cone requires that the ionization cone half-opening angle is less than 25 degrees; this in order to completely hide the counter-cone behind the galaxy disk, which has an inclination of 51° to our line of sight.

An alternative explanation for the large velocities seen in the second component is an outflow produced by an off nuclear starburst. We extracted aperture spectra from the two regions marked with the red circles in the structure map (Fig. 3.1), i.e. the locations of the posited ionization cone and the unseen counter-cone. Fits to these two spectra with *pPXF* show that the stellar templates used in both cases are very similar in terms of stellar population ages. That is, while both require a relatively large fraction of young populations, there is no significant reason to believe that one is significantly younger than the other. [**?**] studied the relation of starburst processes in a sample of twenty Seyfert 2 galaxies by analyzing their near-ultraviolet (looking for high order terms of the Balmer series in absorption) and optical spectra, focusing in the nuclear and circumnuclear regions. They found that the nuclei of spirals galaxies that present

starbursts have a very low excitation ([O III]/H$\beta \leq 1$) which is not the case of our galaxy. For these reasons we disfavor a starburst origin for the second velocity component.

Proceeding with the explanation that the zero-velocity component represents outflowing gas with velocity $\sim$240 km s^{-1} along an ionization cone, it is possible to estimate the mass outflow rate as the ratio between the mass of the outflowing gas and the dynamical time at the nucleus (M_g/t_d). We can obtain the gas mass with:

$$M_g = N_e m_p V\, f \tag{4.1}$$

where N_e is the electron density, m_p is the mass of the proton, V is the volume of the region where the outflow is detected, and f is the filling factor which can be estimated from:

$$L_{H\alpha} \sim f\, N_e^2\, j_{H\alpha}(T) V \tag{4.2}$$

where $j_{H\alpha}(T) = 3.534 \times 10^{-25}$ erg cm^{-3} s^{-1} [75] and $L_{H\alpha}$ is the Hα luminosity emitted by a volume V.

Substituting equation (4.2) into equation (4.1) we obtain:

$$M_g = \frac{m_p\, L_{H\alpha}}{N_e\, j_{H\alpha}(T)} \tag{4.3}$$

If we consider a luminosity distance of 80.7 Mpc, the luminosity of Hα that of our complete FOV ($L_{H\alpha} \approx 2.2 \times 10^{41}$ erg s^{-1}), and assume N_e as the mean value within the inner 0.8 arcsec, centered on the outflow peak ($\sim$ 958 cm^{-3}); we obtain an ionized gas mass of $M_g \approx 5.5 \times 10^5$ M$_\odot$. From the double Gaussian fit we performed in selected apertures (see Sect. 3.2.2), we concluded that almost 70% of the Hα emission comes from the non-rotating component, i.e. a mass of $\sim 3.8{\times}10^5$ M$_\odot$. The dynamical time can be estimated from the ratio between the radius considering the outflow (0.8 arcsec $\approx$ 308 pc) and the velocity of the outflow (assumed as $\sim$ 240 km s^{-1}). This gives $t_d \approx 1.3 \times 10^6$ years and thus the mass outflow rate is $\dot{M}_{out}$ is 0.3 M$_\odot$ yr^{-1}. This value should then be doubled to account for the second, invisible, ionization cone. This outflow rate is $\sim$50 times the estimated accretion rate onto the SMBH in ESO153-G20 (Sect. 3.2.3).

Another notable kinematic feature commented on earlier is the S-shaped isovelocity contours seen in the gas velocity maps, seen most clearly in the Hα and [N II] lines. These S-shaped features are often seen in barred galaxies, and have been explained as pertubations produced by the bar. Since ESO153-G20 shows clear evidence of a bar [RC3; 88] we briefly explore the kinematic signature expected using the linear perturbation analysis outlined in Finlez et al. (submitted). Briefly, this procedure starts with an unperturbed rotation curve based on the mass of the galaxy disk, the photometric parameters of the galaxy (disk and bar PAs, and bar ellipticity) and uses linear perturbation analysis [32, 107, 114] to predict the velocity field expected for different values of bar pattern speed and 'damping' (the smoothing of orbits axis changes at resonance radii). We thus first created an unperturbed velocity field, based on an exponential disk with a total disk mass of $M_d = 1.2 \times 10^{10}$ M$_\odot$, and a disk scalelength $r_d = 0.46$ kpc. [19] gives us an initial $r_d \sim 4.2$ kpc and [63] pointed out a value of $r_d \sim 3.6$ kpc. As a first attempt for the exponential disk, we used a mass value of $1{\times}10^{11}$ M$_\odot$and a disk scalelength certainly lower than the indicated (1 kpc), due to the fact that our center is not at the proper center of the image and thus the fitting code did not converge properly to a solution. This is why some values where chosen "by eye" to fit our data by comparing with the Hα velocity field. We fixed PA_{disk} =10.5°, PA_{bar} = 126 (as obtained from the I band image in [88]) and a bar ellipticity $\epsilon = 0.4$, a mean value obtain after using GALFIT [77] and DISKFIT [92, 100] in the HST image. We perturbated this model following the procedure described in Finlez et al. (submitted), creating a matrix of velocity fields by varying the bar pattern speed over the range 20 to 300 km s^{-1}kpc^{-1} and damping factor λ over the range 0.01 to 0.4.

None of the perturbed models exactly reproduce the S-shaped kinematic pattern seen in the Hα and [N II] emission lines. We therefore did not proceed to the next step of minimizing residuals and thus determining the best-fit bar pertubation model and its associated parameters.

However, some of the perturbed maps did produce roughly the kinematic morphology observed, even if they did not completely recreate the exact S-shape and/or the pertubation amplitudes observed. We show four examples of these 'roughly-matching' bar-perturbed models in Fig. 4.1. Of the four, the one with Ω_p=250 and λ=0.07 appears to most closely follow the observed velocity field, and we plot its predicted velocities in the P-V diagrams in Sect. 3.2.2. Effectively, while we cannot exactly reproduce the distortions in the rotating component of the emission line gas, it is most likely that these are produced due to perturbations by the bar. Unfortunately, this complication means that we are unable to further analyze the rotation component velocity field for signatures of streaming inflows.

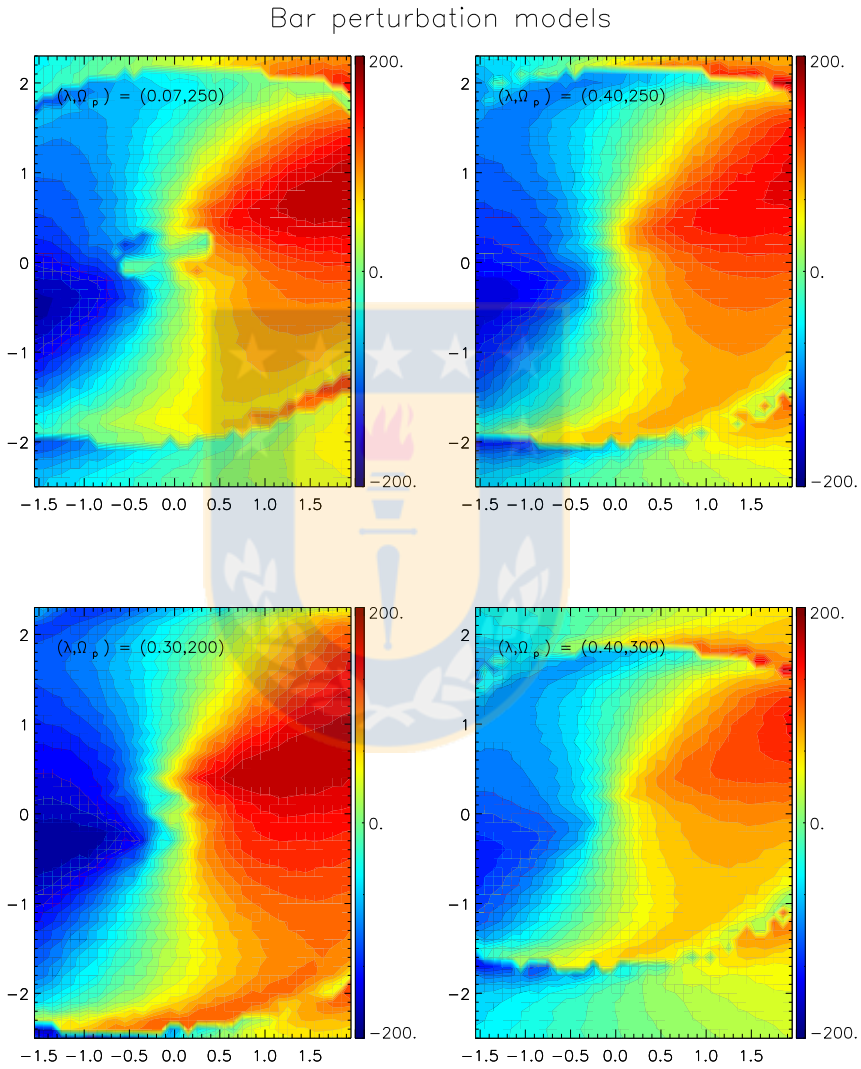

Figure 4.1: Example velocity field models obtained by adding 'bar-pertubations' to an axisymmetric rotation curve. The bar and disk PA, bar ellipticity, and disk mass were fixed to values measured for ESO153-G20, while the bar pattern speed (Ω_p) and damping factor (λ) were varied (see text). Each panel lists the values of Ω_p) and λ and its colors follow the bar on the right. We show only four selected models which are most reminiscent of the observed velocity fields. Image from the author.

Chapter 5

Summary and Conclusions

We have measured the gaseous and stellar kinematics in the inner 1.4×1.9 kpc^2 of the Seyfert 2 galaxy ESO 153-g20 using optical spectra from the GMOS integral field spectrograph on the Gemini South telescope, covering the range 4095-7338 Å, at a spatial resolution of $\approx$ 285 pc and $\sigma_{inst} \approx 36$ km s^{-1}. This allows the detection of prominent emission lines such as Hβ, [O III]$\lambda\lambda$4959,5007, Hα+[N II] $\lambda\lambda$6548,6583 and the [S II] doublet. A series of IDL and Python programs were employed to analyze the lines and obtain spatially resolved radial velocities, velocity dispersions and fluxes. The main results of this work are as follows.

- The stellar velocity field shows circular rotation with an orientation for the line of nodes of $\approx 10.5°$ and reaching amplitudes of ~ 200 km s^{-1}.
- Dust obscuration seen on the structure map, $H\alpha$/Hβ ratios over the FOV and the assumption of trailing spiral arms supports the NE direction as the near side of the galaxy disk.
- Single Gaussian fits to the emission lines show that most of them follow a rotation pattern similar to the stars, slighty shifted on the kinematical center, except for the [O III] emission line, which is dominated by a 'zero-velocity' component that we associated to an outflow in the ionization cone. We attribute the shift on the kinematical center to this outflow.
- High values of [O III]/Hβ ratio (> 10) within a region of 0.8 arcsec diameter, located at 0.25 arcsec SW of the nucleus demonstrate the high ionization caused by AGN emission; while low values (< 4) to the NE demonstrate that rotation dominates on that side.
- Assuming a bi-conical outflow, with one side invisible due to obscuration, a mass outflow rate $\dot{M}_{out} \approx 0.6$ M$_\odot$ yr^{-1} is obtained for ESO 153-G20. These value is significantly higher ($\sim$100 times) than the accretion rate necessary to support the AGN luminosity.
- Bar perturbation models are necessary to reproduce the "S" shape from the Hα velocity field, which due to the single gaussian fit results, and therefore the rotation model for [N II], and the values considered for Ω_p and λ didn't represent the distribution because both components where considered as just one, overvaluing the velocity amplitudes and thus the initial parameters considered for the exponential disk.

Bibliography

[1] Antonucci, R.: 1993, *Annual Rev. Astron. Astrophys.* **31**, 473

[2] Baldwin, J. A., Phillips, M. M., and Terlevich, R.: 1981, *Publ. Astron. Soc. Pac.* **93**, 5

[3] Bamford, S. P., Rojas, A. L., Nichol, R. C., Miller, C. J., Wasserman, L., Genovese, C. R., and Freeman, P. E.: 2008, *MNRAS* **391**, 607

[4] Begelman, M. C., Blandford, R. D., and Rees, M. J.: 1984, *Reviews of Modern Physics* **56**, 255

[5] Bertola, F., Bettoni, D., Danziger, J., Sadler, E., Sparke, L., and de Zeeuw, T.: 1991, *Astrophys. J.* **373**, 369

[6] Bisnovatyi-Kogan, G. S. and Lovelace, R. V. E.: 2001, *New Astronomy Reviews* **45**, 663

[7] Bock, G., Marples, P., and Anderson, J.: 2012, *Central Bureau Electronic Telegrams* 3007

[8] Bosma, A.: 1981, *Astrophysical Journal* **86**, 1825

[9] Bridle, A. H., Hough, D. H., Lonsdale, C. J., Burns, J. O., and Laing, R. A.: 1994, *Astrophysical Journal* **108**, 766

[10] Bridle, A. H. and Perley, R. A.: 1984, *Annual Rev. Astron. Astrophys.* **22**, 319

[11] Buta, R.: 1995, *Astrophys. J., Suppl. Ser.* **96**, 39

[12] Buta, R. and Combes, F.: 1996, *Fundam. Cosmic Phys.* **17**, 95

[13] Buta, R. and Crocker, D. A.: 1991, *Astrophysical Journal* **102**, 1715

[14] Buta, R. and Crocker, D. A.: 1993, *Astrophysical Journal* **105**, 1344

[15] Cappellari, M.: 2017, *MNRAS* **466**, 798

[16] Cappellari, M. and Copin, Y.: 2003, *MNRAS* **342**, 345

[17] Cappellari, M. and Emsellem, E.: 2004, *Publ. Astron. Soc. Pac.* **116**, 138

[18] Cid Fernandes, R., Stasińska, G., Schlickmann, M. S., Mateus, A., Vale Asari, N., Schoenell, W., and Sodré, L.: 2010, *MNRAS* **403**, 1036

[19] Cunow, B.: 2001, *MNRAS* **323**, 130

[20] Curtis, H. D.: 1918, *Publications of Lick Observatory* **13**, 9

[21] da Costa, L. N., Pellegrini, P. S., Davis, M., Meiksin, A., Sargent, W. L. W., and Tonry, J. L.: 1991, *Astrophys. J., Suppl. Ser.* **75**, 935

[22] Davies, R. I., Maciejewski, W., Hicks, E. K. S., Emsellem, E., Erwin, P., Burtscher, L., Dumas, G., Lin, M., Malkan, M. A., Müller-Sánchez, F., Orban de Xivry, G., Rosario, D. J., Schnorr-Müller, A., and Tran, A.: 2014, *Astrophys. J.* **792**, 101

[23] Davies, R. I., Thomas, J., Genzel, R., Müller Sánchez, F., Tacconi, L. J., Sternberg, A., Eisenhauer, F., Abuter, R., Saglia, R., and Bender, R.: 2006, *Astrophys. J.* **646**, 754

[24] de Grijp, M. H. K., Lub, J., and Miley, G. K.: 1987, *Astron. Astrophys. Suppl. Ser.* **70**, 95

[25] de Vaucouleurs, G., de Vaucouleurs, A., Corwin, Jr., H. G., Buta, R. J., Paturel, G., and Fouqué, P.: 1991, *Third Reference Catalogue of Bright Galaxies. Volume I: Explanations and references. Volume II: Data for galaxies between 0^h and 12^h. Volume III: Data for galaxies between 12^h and 24^h.*

[26] Di Matteo, T., Springel, V., and Hernquist, L.: 2005, *Nature* **433**, 604

[27] Dumas, G., Mundell, C. G., Emsellem, E., and Nagar, N. M.: 2007, *MNRAS* **379**, 1249

[28] Englmaier, P. and Shlosman, I.: 2004, *Astrophys. J., Lett.* **617**, L115

[29] Fabian, A. C.: 2012, *Annual Rev. Astron. Astrophys.* **50**, 455

[30] Falcón-Barroso, J., Sánchez-Blázquez, P., Vazdekis, A., Ricciardelli, E., Cardiel, N., Cenarro, A. J., Gorgas, J., and Peletier, R. F.: 2011, *Astron. Astrophys.* **532**, A95

[31] Fathi, K., Storchi-Bergmann, T., Riffel, R. A., Winge, C., Axon, D. J., Robinson, A., Capetti, A., and Marconi, A.: 2006, *Astrophys. J., Lett.* **641**, L25

[32] Fathi, K., van de Ven, G., Peletier, R. F., Emsellem, E., Falcón-Barroso, J., Cappellari, M., and de Zeeuw, T.: 2005, *MNRAS* **364**, 773

[33] Ferrarese, L. and Merritt, D.: 2000, *Astrophys. J., Lett.* **539**, L9

[34] Fischer, T. C., Crenshaw, D. M., Kraemer, S. B., and Schmitt, H. R.: 2013, *Astrophys. J., Suppl. Ser.* **209**, 1

[35] Frank, J., King, A., and Raine, D. J.: 2002, *Accretion Power in Astrophysics: Third Edition*

[36] Gerhard, O. E.: 1993, *MNRAS* **265**, 213

[37] Gimeno, G., Roth, K., Chiboucas, K., Hibon, P., Boucher, L., White, J., Rippa, M., Labrie, K., Turner, J., Hanna, K., Lazo, M., Pérez, G., Rogers, R., Rojas, R., Placco, V., and Murowinski, R.: 2016, in *Ground-based and Airborne Instrumentation for Astronomy VI*, Vol. 9908 of *Proceedings of SPIE*, p. 99082S

[38] Greene, J. E., Zakamska, N. L., and Smith, P. S.: 2012, *Astrophys. J.* **746**, 86

[39] Gültekin, K., Richstone, D. O., Gebhardt, K., Lauer, T. R., Tremaine, S., Aller, M. C., Bender, R., Dressler, A., Faber, S. M., Filippenko, A. V., Green, R., Ho, L. C., Kormendy, J., Magorrian, J., Pinkney, J., and Siopis, C.: 2009, *Astrophys. J.* **698**, 198

[40] Hamuy, M., Suntzeff, N. B., Heathcote, S. R., Walker, A. R., Gigoux, P., and Phillips, M. M.: 1994, *Publ. Astron. Soc. Pac.* **106**, 566

[41] Hamuy, M., Walker, A. R., Suntzeff, N. B., Gigoux, P., Heathcote, S. R., and Phillips, M. M.: 1992, *Publ. Astron. Soc. Pac.* **104**, 533

[42] Häring, N. and Rix, H.-W.: 2004, *Astrophys. J., Lett.* **604**, L89

[43] Heckman, T. M.: 1980, *Astron. Astrophys.* **87**, 152

[44] Hernquist, L.: 1989, *Nature* **340**, 687

[45] Ho, L. C., Filippenko, A. V., and Sargent, W. L. W.: 1993, *Astrophys. J.* **417**, 63

[46] Ho, L. C., Filippenko, A. V., and Sargent, W. L. W.: 1997, *Astrophys. J., Suppl. Ser.* **112**, 315

[47] Hopkins, P. F. and Quataert, E.: 2010, *MNRAS* **407**, 1529

[48] Hubble, E. P.: 1926, *Astrophys. J.* 64

[49] Karouzos, M., Im, M., Trichas, M., Goto, T., Malkan, M., Ruiz, A., Jeon, Y., Kim, J. H., Lee, H. M., Kim, S. J., Oi, N., Matsuhara, H., Takagi, T., Murata, K., Wada, T., Wada, K., Shim, H., Hanami, H., Serjeant, S., White, G. J., Pearson, C., and Ohyama, Y.: 2014, *Astrophys. J.* **784**, 137

[50] Kauffmann, G., Heckman, T. M., Tremonti, C., Brinchmann, J., Charlot, S., White, S. D. M., Ridgway, S. E., Brinkmann, J., Fukugita, M., Hall, P. B., Ivezić, Ž., Richards, G. T., and Schneider, D. P.: 2003, *MNRAS* **346**, 1055

[51] Keeler, J. E.: 1908, *Publications of Lick Observatory* **8**, 1

[52] Kewley, L. J., Groves, B., Kauffmann, G., and Heckman, T.: 2006, *MNRAS* **372**, 961

[53] Kewley, L. J., Maier, C., Yabe, K., Ohta, K., Akiyama, M., Dopita, M. A., and Yuan, T.: 2013, *Astrophys. J., Lett.* **774**, L10

[54] Knapen, J. H.: 2005, *Astrophys. Space. Sci.* **295**, 85

[55] Kormendy, J. and Gebhardt, K.: 2001, in J. C. Wheeler and H. Martel (eds.), *20th Texas Symposium on relativistic astrophysics*, Vol. 586 of *American Institute of Physics Conference Series*, pp 363–381

[56] Krajnović, D., Cappellari, M., de Zeeuw, P. T., and Copin, Y.: 2006, *MNRAS* **366**, 787

[57] Krist, J. E., Hook, R. N., and Stoehr, F.: 2011, in *Optical Modeling and Performance Predictions V*, Vol. 8127 of *Proceedings of SPIE*, p. 81270J

[58] Lauberts, A.: 1982, *ESO/Uppsala survey of the ESO(B) atlas*

[59] Lauberts, A. and Valentijn, E. A.: 1989, *The surface photometry catalogue of the ESO-Uppsala galaxies*

[60] Lena, D., Robinson, A., Storchi-Bergman, T., Schnorr-Müller, A., Seelig, T., Riffel, R. A., Nagar, N. M., Couto, G. S., and Shadler, L.: 2015, *Astrophys. J.* **806**, 84

[61] Lin, M.-Y., Davies, R. I., Burtscher, L., Contursi, A., Genzel, R., González-Alfonso, E., Graciá-Carpio, J., Janssen, A., Lutz, D., Orban de Xivry, G., Rosario, D., Schnorr-Müller, A., Sternberg, A., Sturm, E., and Tacconi, L.: 2016, *MNRAS* **458**, 1375

[62] Lynden-Bell, D.: 1969, *Nature* **223**, 690

[63] Ma, J., Peng, Q.-H., Chen, R., and Ji, Z.-H.: 1997, *Astron. Astrophys. Suppl. Ser.* **126**, 503

[64] Maciejewski, W.: 2004, *MNRAS* **354**, 892

[65] Mediavilla, E. and Arribas, S.: 1993, *Nature* **365**, 420

[66] Morganti, R., Holt, J., Saripalli, L., Oosterloo, T. A., and Tadhunter, C. N.: 2007, *Astron. Astrophys.* **476**, 735

[67] Müller Sánchez, F., Davies, R. I., Eisenhauer, F., Tacconi, L. J., Genzel, R., and Sternberg, A.: 2006, *Astron. Astrophys.* **454**, 481

[68] Müller-Sánchez, F., Prieto, M. A., Hicks, E. K. S., Vives-Arias, H., Davies, R. I., Malkan, M., Tacconi, L. J., and Genzel, R.: 2011, *Astrophys. J.* **739**, 69

[69] Murayama, T. and Taniguchi, Y.: 1998, *Astrophys. J., Lett.* **497**, L9

[70] Nesvadba, N. P. H., Polletta, M., Lehnert, M. D., Bergeron, J., De Breuck, C., Lagache, G., and Omont, A.: 2011, *MNRAS* **415**, 2359

[71] Netzer, H.: 2006, in D. Alloin (ed.), *Physics of Active Galactic Nuclei at all Scales*, Vol. 693 of *Lecture Notes in Physics, Berlin Springer Verlag*, p. 1

[72] Netzer, H.: 2015, *Annual Rev. Astron. Astrophys.* **53**, 365

[73] Nevin, R., Comerford, J., Müller-Sánchez, F., Barrows, R., and Cooper, M.: 2016, *Astrophys. J.* **832**, 67

[74] Osterbrock, D. E.: 1977, *Astrophys. J.* **215**, 733

[75] Osterbrock, D. E.: 1989, *Astrophysics of gaseous nebulae and active galactic nuclei*

[76] Paturel, G., Petit, C., Prugniel, P., Theureau, G., Rousseau, J., Brouty, M., Dubois, P., and Cambrésy, L.: 2003, *Astron. Astrophys.* **412**, 45

[77] Peng, C. Y., Ho, L. C., Impey, C. D., and Rix, H.-W.: 2002, *Astrophysical Journal* **124**, 266

[78] Perrine, C. D.: 1922, *MNRAS* **82**, 486

[79] Peterson, B. M.: 1997, *An Introduction to Active Galactic Nuclei*

[80] Pogge, R. W. and Martini, P.: 2002, *Astrophys. J.* **569**, 624

[81] Reunanen, J., Kotilainen, J. K., and Prieto, M. A.: 2003, *MNRAS* **343**, 192

[82] Ricci, C., Walter, R., Courvoisier, T. J.-L., and Paltani, S.: 2011, *Astron. Astrophys.* **532**, A102

[83] Riffel, R. A.: 2010, *Astrophys. Space. Sci.* **327**, 239

[84] Rodríguez-Ardila, A., Viegas, S. M., Pastoriza, M. G., and Prato, L.: 2002, *Astrophys. J.* **579**, 214

[85] Rupke, D. S. N. and Veilleux, S.: 2011, *Astrophys. J., Lett.* **729**, L27

[86] Sánchez-Blázquez, P., Peletier, R. F., Jiménez-Vicente, J., Cardiel, N., Cenarro, A. J., Falcón-Barroso, J., Gorgas, J., Selam, S., and Vazdekis, A.: 2006, *MNRAS* **371**, 703

[87] Schmitt, H. R., Donley, J. L., Antonucci, R. R. J., Hutchings, J. B., and Kinney, A. L.: 2003, *Astrophys. J., Suppl. Ser.* **148**, 327

[88] Schmitt, H. R. and Kinney, A. L.: 2000, *Astrophys. J., Suppl. Ser.* **128**, 479

[89] Schnorr-Müller, A., Storchi-Bergmann, T., Nagar, N. M., and Ferrari, F.: 2014a, *MNRAS* **438**, 3322

[90] Schnorr-Müller, A., Storchi-Bergmann, T., Nagar, N. M., Robinson, A., Lena, D., Riffel, R. A., and Couto, G. S.: 2014b, *MNRAS* **437**, 1708

[91] Schnorr Müller, A., Storchi-Bergmann, T., Riffel, R. A., Ferrari, F., Steiner, J. E., Axon, D. J., and Robinson, A.: 2011, *MNRAS* **413**, 149

[92] Sellwood, J. A. and Sánchez, R. Z.: 2010, *MNRAS* **404**, 1733

[93] Seyfert, C. K.: 1943, *Astrophys. J.* **97**, 28

[94] Shakura, N. I. and Sunyaev, R. A.: 1973, in H. Bradt and R. Giacconi (eds.), *X- and Gamma-Ray Astronomy*, Vol. 55 of *IAU Symposium*, p. 155

[95] Simões Lopes, R. D., Storchi-Bergmann, T., de Fátima Saraiva, M., and Martini, P.: 2007, *Astrophys. J.* **655**, 718

[96] Skrutskie, M. F., Cutri, R. M., Stiening, R., Weinberg, M. D., Schneider, S., Carpenter, J. M., Beichman, C., Capps, R., Chester, T., Elias, J., Huchra, J., Liebert, J., Lonsdale, C., Monet, D. G., Price, S., Seitzer, P., Jarrett, T., Kirkpatrick, J. D., Gizis, J. E., Howard, E., Evans, T., Fowler, J., Fullmer, L., Hurt, R., Light, R., Kopan, E. L., Marsh, K. A., McCallon, H. L., Tam, R., Van Dyk, S., and Wheelock, S.: 2006, *Astrophysical Journal* **131**, 1163

[97] Slipher, V. M.: 1914, *Lowell Observatory Bulletin* **2**, 66

[98] Sofue, Y. and Rubin, V.: 2001, *Annual Rev. Astron. Astrophys.* **39**, 137

[99] Sparke, L. S. and Gallagher, III, J. S.: 2007, *Galaxies in the Universe*

[100] Spekkens, K. and Sellwood, J. A.: 2007, *Astrophys. J.* **664**, 204

[101] Storchi-Bergmann, T., Dors, Jr., O. L., Riffel, R. A., Fathi, K., Axon, D. J., Robinson, A., Marconi, A., and Östlin, G.: 2007, *Astrophys. J.* **670**, 959

[102] Storchi-Bergmann, T., Lopes, R. D. S., McGregor, P. J., Riffel, R. A., Beck, T., and Martini, P.: 2010, *MNRAS* **402**, 819

[103] Sturm, E., González-Alfonso, E., Veilleux, S., Fischer, J., Graciá-Carpio, J., Hailey-Dunsheath, S., Contursi, A., Poglitsch, A., Sternberg, A., Davies, R., Genzel, R., Lutz, D., Tacconi, L., Verma, A., Maiolino, R., and de Jong, J. A.: 2011, *Astrophys. J., Lett.* **733**, L16

[104] Tadhunter, C.: 2008, *New Astronomy Reviews* **52**, 227

[105] Treister, E., Schawinski, K., Urry, C. M., and Simmons, B. D.: 2012, *Astrophys. J., Lett.* **758**, L39

[106] Urry, C. M. and Padovani, P.: 1995, *Publ. Astron. Soc. Pac.* **107**, 803

[107] van de Ven, G. and Fathi, K.: 2010, *Astrophys. J.* **723**, 767

[108] van der Kruit, P. C. and Allen, R. J.: 1978, *Annual Rev. Astron. Astrophys.* **16**, 103

[109] van der Marel, R. P. and Franx, M.: 1993, *Astrophys. J.* **407**, 525

[110] van Dokkum, P. G., Bloom, J., and Tewes, M.: 2012, *L.A.Cosmic: Laplacian Cosmic Ray Identification*, Astrophysics Source Code Library

[111] Vazdekis, A., Sánchez-Blázquez, P., Falcón-Barroso, J., Cenarro, A. J., Beasley, M. A., Cardiel, N., Gorgas, J., and Peletier, R. F.: 2010, *MNRAS* **404**, 1639

[112] Wolf, M.: 1914, *Vierteljahresschrift Astron. Gesell* **49**, 162

[113] Woltjer, L.: 1959, *Astrophys. J.* **130**, 38

[114] Wong, T., Blitz, L., and Bosma, A.: 2004, *Astrophys. J.* **605**, 183

[115] Xiao, T., Barth, A. J., Greene, J. E., Ho, L. C., Bentz, M. C., Ludwig, R. R., and Jiang, Y.: 2011, *Astrophys. J.* **739**, 28